České vysoké učení technické v Praze
Fakulta strojní

Ústav materiálového inženýrství

Slitina NiTi s tvarovou pamětí připravená technologií RF-ICP

RF-ICP deposition of NiTi shape memory alloy

BAKALÁŘSKÁ PRÁCE

Vypracoval: Noé Elis
Vedoucí práce: doc. Ing. Jan Čížek, Ph.D.
Rok: 2024

ZADÁNÍ BAKALÁŘSKÉ PRÁCE

I. OSOBNÍ A STUDIJNÍ ÚDAJE

Příjmení: **Elis** Jméno: **Noé** Osobní číslo: **509138**

Fakulta/ústav: **Fakulta strojní**

Zadávající katedra/ústav: **Ústav materiálového inženýrství**

Studijní program: **Teoretický základ strojního inženýrství**

Studijní obor: **bez oboru**

II. ÚDAJE K BAKALÁŘSKÉ PRÁCI

Název bakalářské práce:

Slitina NiTi s tvarovou pamětí připravená technologií RF-ICP

Název bakalářské práce anglicky:

RF-ICP deposition of NiTi shape memory alloy

Pokyny pro vypracování:

1. Vypracujte rešerši o základních charakteristikách technologie RF-ICP a fenoménu tvarové paměti.
2. Naneste zvolené prášky Ni-Ti za zvolených hodnot depozičních parametrů pomocí RF-ICP.
3. Proveďte mikrostrukturní a chemickou analýzu získaných nástřiků.
4. Získané výsledky porovnejte s literaturou.

Seznam doporučené literatury:

1. Davis: Handbook of Thermal Spray Technology. ASM International, 2004.
2. Boulos: RF induction plasma spraying: state-of-the-art review. J Therm Spray Technol, 1, 1992, 33.
3. Jani, Leary, Subic, Gibson: A review of shape memory alloy research, applications and opportunities. Mater Design, 56, 2014, 1078.
4. Mauer, Rauwald, Sohn, Weirich: Cold gas spraying of nickel-titanium coatings for protection against cavitation. J Therm Spray Technol, 30, 2021, 131.
5. Samal, Tyc, Cizek, Klecka, Lukac, Molnarova, de Prado, Weiss, Kopecek, Heller, Sittner, Chraska: Fabrication of Thermal Plasma Sprayed NiTi Coatings Possessing Functional Properties. Coatings, 11, 2021, 610.

Jméno a pracoviště vedoucí(ho) bakalářské práce:

doc. Ing. Jan Čížek, Ph.D. Ústav materiálového inženýrství

Jméno a pracoviště druhé(ho) vedoucí(ho) nebo konzultanta(ky) bakalářské práce:

Datum zadání bakalářské práce: **12.03.2024** Termín odevzdání bakalářské práce: **21.07.2024**

Platnost zadání bakalářské práce: _____

doc. Ing. Jan Čížek, Ph.D. podpis vedoucí(ho) práce	doc. Ing. Ladislav Cvrček, Ph.D. podpis vedoucí(ho) ústavu/katedry	doc. Ing. Miroslav Španiel, CSc. podpis děkana(ky)

III. PŘEVZETÍ ZADÁNÍ

Student bere na vědomí, že je povinen vypracovat bakalářskou práci samostatně, bez cizí pomoci, s výjimkou poskytnutých konzultací. Seznam použité literatury, jiných pramenů a jmen konzultantů je třeba uvést v bakalářské práci.

. _____
Datum převzetí zadání

_____
Podpis studenta

Prohlášení

Prohlašuji, že jsem svou bakalářskou práci vypracoval samostatně a použil jsem pouze podklady (literaturu, projekty, SW atd.) uvedené v přiloženém seznamu.

V Praze dne ....

Noé Elis

Poděkování

Děkuji doc. Ing. Janu Čížkovi, Ph.D. za vedení mé bakalářské práce, za podnětné návrhy, které ji obohatily, a za to jakou vřelou a přátelskou podporou pro mě byl. Děkuji také Ing. Lukáši Babkovi za přátelské konzultace a za výpomoc při experimentální části. Za výpomoc při experimentální části děkuji také Ing. Jakubu Klečkovi, RNDr. Františku Lukáčovi, Ph.D a Ing. Petru Králíčkovi.

"It ain't much, but it's honest work." - David Brandt

Noé Elis

Anotace

Tato bakalářská práce se zabývá depozicí povrchových nástřiků slitiny niklu a titanu se schopností tvarové paměti na ocelové substráty za využití technologie radiofrekvenčního indukčně vázaného plazmatu. Cílem práce bylo nanést dva zvolené, odlišné nikl-titanové prášky za identických hodnot depozičních parametrů a provést mikrostrukturní a chemickou analýzu takto získaných nástřiků. Získané výsledky byly následně diskutovány a porovnány s dostupnou literaturou.

Klíčová slova

nitinol, nikl, titan, nástřik, tvarová paměť, RF-ICP, radiofrekvenční indukčně vázané plazma, mikrostruktura, SEM, EDX, XRD

Annotation

This bachelor thesis deals with the deposition of nickel-titanium alloy coatings with shape memory capability on steel substrates using radio frequency inductively-coupled plasma technology. The work aimed to deposit two selected, different nickel-titanium powders under identical deposition parameters and perform microstructural and chemical analysis of the resulting coatings. The results obtained were then discussed and compared with the available literature.

Keywords

nitinol, nickel, titanium, coating, shape memory effect, RF-ICP, radio frequency inductively-coupled plasma, microstructure, SEM, EDX, XRD

Contents

Chapter 1

Introduction

Shape memory alloys are known for their unique ability to return to a predefined shape when subjected to external stimuli. Among them, nickel-titanium (NiTi), or nitinol, is especially valued for its shape memory and superelastic properties. This bachelor thesis explores the deposition of NiTi shape memory alloys in the form of surface coatings, focusing on the radio frequency inductively-coupled plasma (RF-ICP) method.

Two types of NiTi coatings were prepared on steel substrates. Both were deposited using the same RF-ICP parameters but originated from different initial powders with varying morphologies. The initial powders and deposited coatings were then analyzed using scanning electron microscopy, energy dispersive X-ray spectroscopy, and X-ray diffraction to study their microstructure and chemical and phase composition.

This research showed that the initial powder properties strongly affected the deposited coating properties. More importantly, the RF-ICP proved to be a well-suited method for NiTi deposition due to its controlled atmosphere character, leading to the absence of oxides. These results offer insights that can guide future work in applications where shape memory and superelasticity are critical.

Chapter 2

Literature review

This section describes the phenomenon of the shape memory effect along with its principles, materials that exhibit these capabilities, their current and potential uses and applications. In the second part, thermally sprayed coatings are introduced, especially plasma spray processes followed by a more detailed description of the radio frequency inductively-coupled plasma spray process, as this method was used during our experiment.

2.1 Shape memory alloys

2.1.1 General description

Shape memory alloys (SMA) are a type of metallic alloys known for their unique ability to return to their original shape, size, and form by the influence of temperature or a magnetic field after being deformed by an external force. This behavior is known as the shape memory effect (SME) [1].

The first SMA were discovered in the early 1930s by a Swedish physicist Arne Ölander. He found that if a gold-cadmium alloy is plastically deformed in a cold state and then heated to a certain temperature, the alloy will return to its original shape. More instances of such behavior were reported by researchers in the following years. Combinations such as copper-zinc, copper-tin, or indium-thallium became the first known SMA and have continued to interest scientists ever since. The first practical applications came after the discovery of nickel-titanium SMA by William Buehler and Frederick Wang in 1962 in Maryland, USA. Nowadays, SMA are primarily used in biomechanics, aerospace, robotics, and automotive industries [1, 2, 3].

2.1.2 Principles

The internal structure of SMA is the key to their behavior, comprising martensitic and austenitic phases. Both are interstitial solid-state solutions and while austenite is relatively softer, more malleable, and stable at high temperatures, martensite is harder and more stable at low temperatures. The austenite has a face-centered cubic crystal structure, whereas martensite can exist in two types of monoclinic crystal structures: twinned (undeformed martensite) and detwinned (plastically deformed martensite), see Fig. 2.1. SME refers to a diffusion-less solid phase transition between the austenite and martensite crystal structures [1, 2, 4].

If we deform SMA while in the martensitic state, it retains this deformation and holds a certain shape. Upon heating, the martensite begins transforming into the austenite phase at the austenite-start-temperature (A_s). The transformation completes at the austenite-finish-temperature (A_f), marking the end of the process. Between A_s and A_f, SMA returns to its original shape. In reverse, during cooling, martensitic structures begin to form at the martensite-start-temperature (M_s) and complete at the martensite-finish-temperature (M_f). Above a certain temperature called M_d, the SMA is deformed permanently, and martensitic structure can no longer be stress induced. This process exhibits thermal hysteresis dependent on temperature, stress, strain, and the thermodynamic properties of SMA [1, 5].

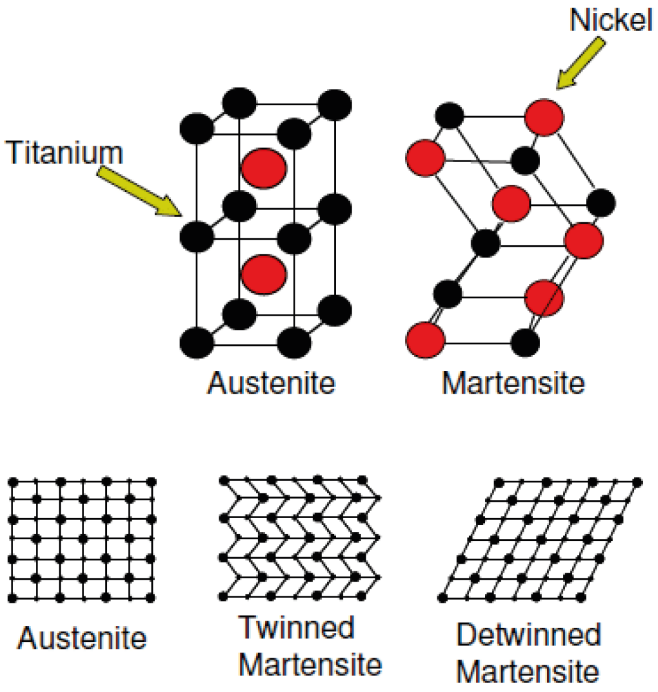

Figure 2.1: Austenite/martensite crystal structure of NiTi SMA [6]

Another phenomenon associated with SMA is known as pseudoelasticity (PE) or superelasticity (SE). This is a reversible response to applied forces caused by the described phase transformation. The thermal hysteresis can be displayed using hysteresis loop diagrams related to the SME. They are practical tools when selecting the right alloy for various applications. For instance, for faster actuators with smaller working loads, it is common to have a smaller hysteresis. For tasks that require retaining a set shape across a wide temperature range, as seen in deployable structures and similar applications, a larger hysteresis is necessary [1, 5].

All the shape-changing effects can be divided into three shape memory characteristics:

- One-way shape memory effect (**OWSME**), which stays in the deformed shape after removal of external force and recovers back to the original shape upon heating.
- Two-way shape memory effect (**TWSME**), which is reversible SME and can remember its shape at both low and high temperatures, in contrast to OWSME,

which can only remember its shape at high temperatures.

- Superelasticity/pseudoelasticity, where a material can return to its undeformed shape after mechanical loading is applied between A_f and M_d temperatures even without any external stimuli (thermal activation). High elastic (reversible) deformations occur.

2.1.3 Materials with shape memory effect

Ceramics are generally very hard materials with good wear and corrosion resistance. Ceramic SME materials (SMC) have great potential in the biomedical industry, especially Zr-based ceramics. Mechanical damping, actuation, and sensing properties were discovered in association with the superelastic behavior of these types of ceramics. Zr-based SMC exhibited a stress-induced strain of nearly 1%, with possible improvement of fatigue resistance and strain properties based on the modification of their internal structure [7, 8].

Polymers are a special group of materials with SME. They are made of polymer chains held together by crosslinks/bonds. These bonds contribute to their properties and influence their behavior and SME. Compared to metal alloys and ceramics, SME polymers can be triggered by a wider range of stimuli. They can be described mainly as OWSME, because TWSME polymers are still rare despite recent research. Typically, they exhibit a minimum of two different phases, in which the first one sets the original shape, usually during the manufacturing process, while the second one stabilizes the temporary shape by either glass transition, crystallization, transitions between liquid crystalline phases, or reversible covalent/non-covalent bonds. Applications of such polymers are smart fabrics, implants, shrinkable tubes, or intelligent medical devices [9, 10].

Composites blend the properties of different SME materials to accomplish various functions and to take advantage of their particular strengths. Integrating the SME materials into the composite matrices enhances the composites functionality. SME composites gained international attention in recent years as a promising smart material systems. Easily shaped into diverse forms they allowed the production of varied composites using continuous and discontinuous reinforcements, and found applications in shape control and vibration management, particularly in thermoplastic and thermoset polymer matrix composites [11].

Metals and their compounds are the best-known materials with SME, common for most commercial applications. Thanks to the many combinations of different elements, specific requirements for designated applications can be met. Metals have good mechanical properties and can be easily manufactured. They can withstand high working loads and have relatively high Young's modulus. Among the best-known representatives of SMA are the following groups:

- **Fe-based** SME alloys are mostly used in the construction industry as fasteners, joints, couplings, etc. They have excellent low-cycle fatigue resistance, which is crucial for reliability. They are also used with an admixture of chromium and nickel (to form a protective layer by passivation) as an equivalent to stainless steel in aggressive chloride environments close to the shore or in the sea. Fe-based SMA are also relatively cheap to produce and thus popular among

civil engineers, where construction parts have bigger dimensions and need to be financially bearable [12].

- **Cu-based** SME alloys are used in applications with higher working temperatures and are particularly popular thanks to their large range of working temperatures and lower cost of manufacturing. On the other hand, at room temperature, the Cu-based SMA are relatively brittle and have low deformation [13].
- **NiTi-based** SME alloys are attractive in the biomedical, aerospace, and robotics industries. NiTi-based SMA have many practical applications based on their good mechanical properties, including low density, higher Young's modulus, and good corrosion resistance. Especially in the biomedical industry, NiTi alloys are used for implants with good biocompatibility, for example medical stents, as shown in Fig. 2.2. Modern manufacturing methods for producing NiTi-based SMA include additive technology, which can improve the speed of production of parts, produce protective coatings, reduce raw material usage, and support manufacturing sustainability [1, 14, 15, 16].

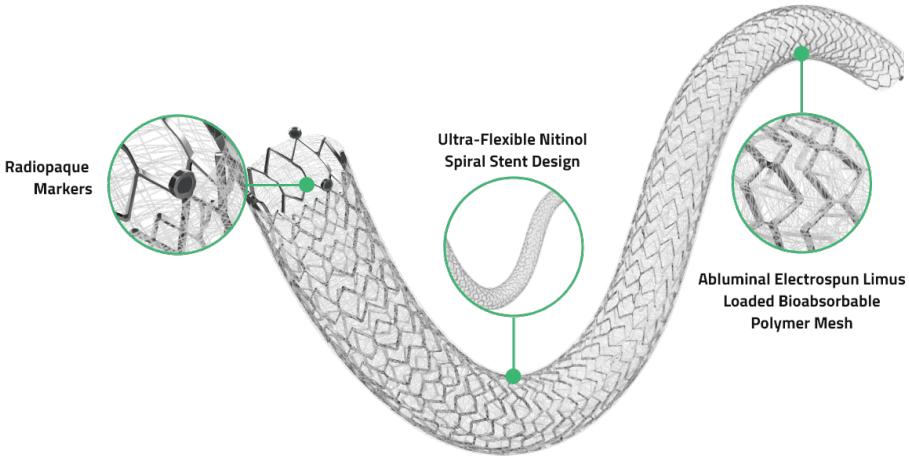

Figure 2.2: Medical stent made of NiTi-based SMA (nitinol) developed by Medinol company (Israel) [17].

2.1.4 Potential applications of NiTi SMA

Owing to their unparalleled material properties, NiTi SMA are widely used today. They are mainly manufactured by conventional methods but because of their high ductility and reactivity, they suffer from poor workability during the processing, and it is hard to produce more complex shapes other than wires, tubes, or sheets. The casting routes, although offering a wider variety of shapes through the procedure and subsequent milling, are generally energy-intensive. They have a high rate of oxygen and carbon contamination, which affects the shape memory and superelastic effects. Additive manufacturing methods (AM) could eliminate these imperfections. A big advantage of AM is the ability to produce the materials from relatively thin coatings to entire parts of various shapes [18].

Potential applications for NiTi SMA as coatings made by AM are primarily based on the SE properties and chemical composition. Components or parts can take advantage of these properties and extend their life expectancy or improve their functionality. For example, NiTi coatings on propellers, turbines, or their components, increase wear resistance or anti-cavitation endurance, where the coating absorbs the energy from collapsing cavitation bubbles on the component's surface. This is closely connected with SE, where the ability of high elastic deformations protects the part from damage. Based on this analogy, there is a possibility of a wider application of NiTi coatings [19, 20].

2.2 Thermally sprayed coatings

Coatings can provide solutions for enhancing the surface properties of numerous components across various industries. For proper functionality, the coatings must be of high quality, with good adhesion as well as chemical and thermal expansion compatibility with the substrate or the component. These requirements can be achieved through careful selection of the coating materials and the appropriate choice of the manufacturing methods. One of the options for producing high-quality coatings are thermal spray technologies [21].

2.2.1 Basic principles

Compared to other surface processes that operate at the atomic or molecular level, thermal spray methods can deposit relatively thick coatings of up to several mm thickness over large areas in a short amount of time. In these processes, the coating material can be supplied in the form of powder (the most commonly used feedstock and will be addressed in the following text), wires, or rods, which is then melted into droplets. These droplets are then propelled by process gases towards the substrate. Upon impact on the surface, the droplets spread, adhere to the substrate, cool down, and solidify to produce thin lamellae called splats. The wide operating temperature range of thermal spray methods allows for the application of various coating materials [21].

The main variables influencing the quality and properties of thermally sprayed coatings are the in-flight velocity and temperature of the feedstock material particles. These are, in turn, influenced by the dwell time of the particles, i.e., the time from when the particle enters the gas stream until it hits the substrate. During dwell time, the temperature of propelled particles rises, and their velocity is influenced by the flow of the surrounding gases. We can adjust the dwell time by modifying factors such as the distance of the nozzle from the substrate, the location of the powder-feed entry point (external/internal), the speed of the gases, the particle size, etc. [21].

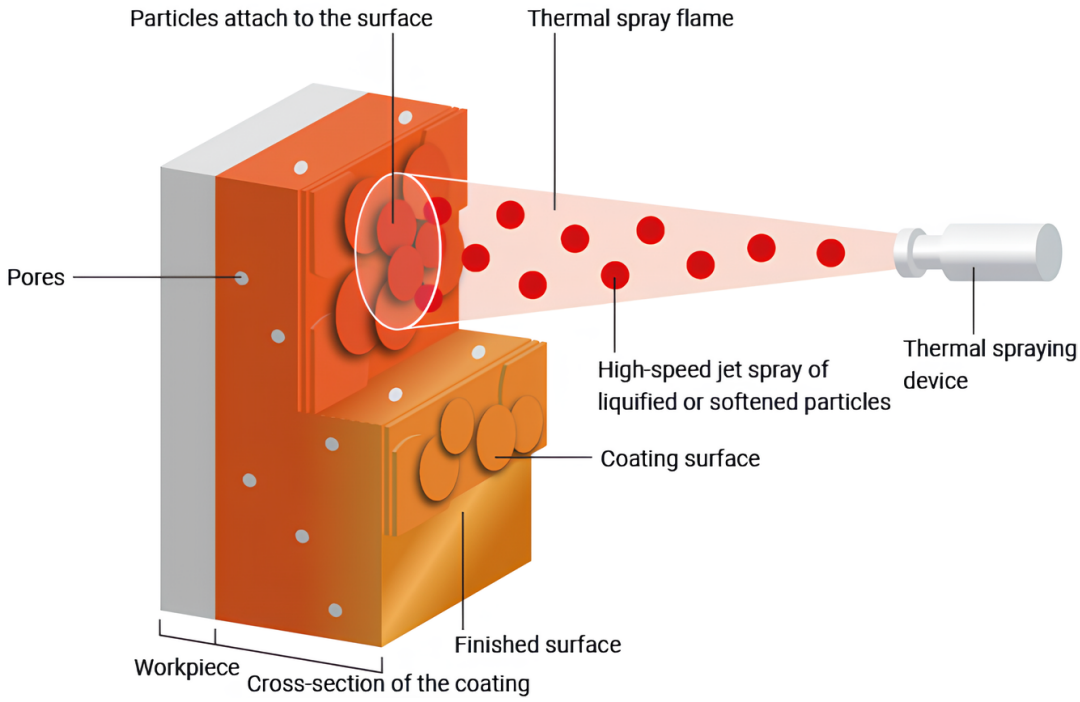

Figure 2.3: Illustration of the coating process using thermal spray [22].

Thermal spray processes can be basically differentiated into two main groups based on the method of heat generation, as illustrated in Fig 2.4. A brief summary of the most commonly used thermal spray processes is provided in the following text [21, 23, 24, 25]:

- **Flame spray** is an early thermal spray process that melts and propels feedstock using a flame generated from a mixture of oxygen and combustion fuel gases such as acetylene. Coatings from this process typically have lower density and often contain oxide particles due to interaction with the oxygen gas.

- **Detonation gun** process is in principle similar to flame spray. However, it achieves denser coatings with low porosity by confining the combustion process within a closed long tube that acts as a barrel, which opens only upon reaching a certain pressure inside the barrel. After opening, the particles reach up to supersonic velocities. This non-continuous deposition process typically works at a frequency of around 10 Hz.

- **High-velocity oxyfuel spray** (HVOF) process is similar to a detonation gun, but with continuous combustion. It uses kerosene and air/oxygen, with high chamber pressures, and supersonic particle speeds achieved by the application of the de Laval nozzle. HVOF coatings are dense and have a low porosity.

- Instead of burning fuel like the previous methods, **wire arc spray** (WAS) melts feedstock wires using an electric arc between them. A flow of room-temperature gas is then used to propel the molten material toward a substrate. The conductive feedstock requirement limits material choices, but due to the ambient temperature of process gas, the method allows for coating on e.g. polymers, fiberglass, or wood. WAS has one of the lowest particle speeds, resulting in coatings of lower density, similar to flame spray.

- **Plasma spray** is a different thermal spray process that uses plasma (a mix of electrons, ions, and neutral atoms) to generate high heat which melts the feedstock particles. These are then propelled toward a substrate by gases exiting from a plasma torch. These gases, in which the plasma spray operates, are plasma-forming gases like argon, helium, or hydrogen, offering high temperatures, and a wide range of achievable coating porosity. Plasma spray operates in controller chambers, e.g. for low-oxide depositions, or in the open air. In the case of the open-air atmosphere, the plasma-forming gases are present only in the plasma torch and subsequently in the plasma stream. Thanks to these various properties, plasma spray is suitable for many engineering applications.

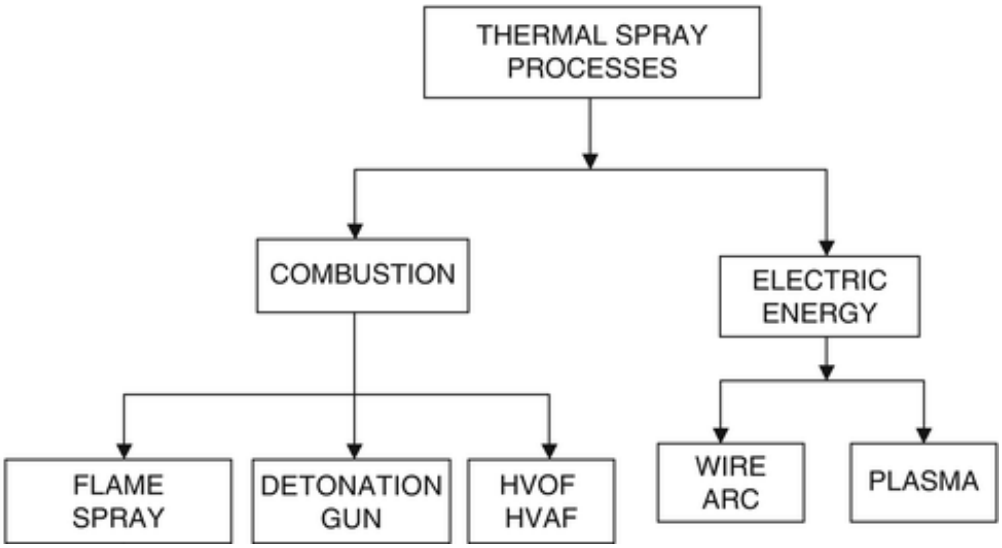

Figure 2.4: Thermal spray groups and the individual processes (edited from [23]).

2.2.2 RF-ICP

Plasma spray differs significantly from the other thermal spray processes. The heat required to melt feedstock particles is not generated by combustion. Instead, it is generated when the plasma electrons and ions generated in the plasma torch recombine upon leaving the torch orifice. Subsequently, the molten particles are accelerated toward the substrate by the flowing (now electrically neutral) gases of high temperature. The energy sources for generating the plasma typically include DC (direct current) or AC (alternating current) electric arcs, and radio frequency (RF) discharges.

Radio frequency inductively-coupled plasma method (RF-ICP) began to see wider commercial use in the field of coatings in the 1980s, thanks to the possibility of inert atmosphere deposition and the absence of (consumable) electrodes, which are normally present in the other plasma generation processes. Since then, the method progressed both in the manufacturing sector and in research. RF-ICP utilizes an oscillating RF field, generated by induction coils within the torch, to create, couple, and inductively heat the plasma stream. Once the electromagnetic field is established, the flowing medium (composed of various gases, usually argon, helium, hydrogen, and their combinations) is ignited using an ignition coil. Free electrons begin to form and, while accelerated by the electromagnetic field, they collide with

surrounding atoms, heating them to their ionizing temperature by transferring their kinetic energy. Subsequently, these atoms release their electrons, initiating a chain reaction that leads to the formation of ICP.

RF-ICP systems run on an RF power supply (PS). In smaller installations, the PS is typically under 100 kW. For these systems, the frequency at which the AC in the coils oscillates ranges between 2–4 MHz, while in larger installations with PS greater than 100 kW, frequencies can be as low as 0.2 MHz. The minimum required power depends on four main parameters: plasma gas properties, oscillator frequency, operating pressure, and discharge size.

PS supplies energy to the plasma torch. The plasma torch is enclosed in a water-cooled confinement tube with process gases flowing through the torch. The process gases are fed axially into the plasma torch, divided into three sections. Sheath gas is supplied along the tube walls for their protection from the heat. Carrier gas transports the powder feedstock into the process and is fed directly into the middle of the tube. Finally, central gas is used to form, stabilize, and direct the plasma stream and is supplied between these two sections. Proper cooling of the torch is crucial for its durability and to maintain temperatures inside the tube for ideal particle melting. A detailed scheme of an RF-ICP torch with real-life reference photography is shown in Fig. 2.5 [21, 24].

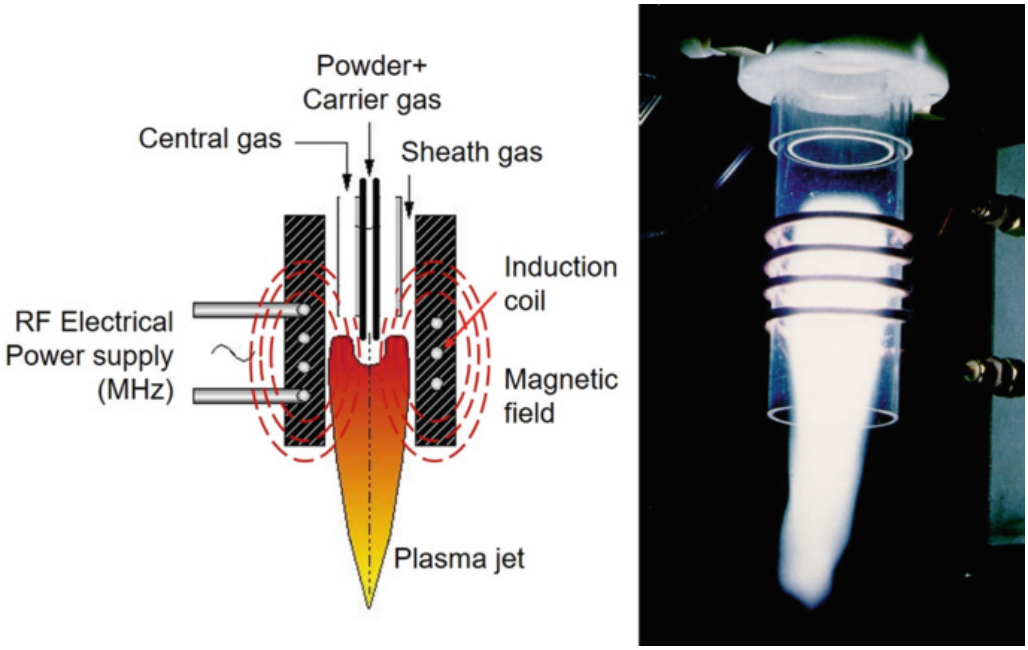

Figure 2.5: RF-ICP torch scheme (left) and real process (right) [25].

In our study, the RF-ICP was applied for the deposition of NiTi coatings in order to assess the suitability and applicability of the selected process for the task, as well as to examine the microstructure as well as changes to the chemical and phase composition of the coatings. And to discuss future developments in manufacturing SME coatings with a focus on the SE.

Chapter 3

Experimental setup

In this section, the experimental setup will be described. The deposition of NiTi coating was carried out using a 15 kW RF-ICP system from two types of feedstock NiTi powders, and the powders as well as the deposits were characterized by scanning electron microscope (SEM), energy dispersive X-ray (EDX), and X-ray diffraction (XRD) methods.

3.1 Feedstock powders

Two types of NiTi powders were used in our experiment to verify the flexibility of the RF-ICP process for the preparation of NiTi coatings and the sensitivity of the result to the initial powders. The first powder was manufactured by E.O. Paton Electric Welding Institute in Kyiv, Ukraine, and will be labeled as **S1** in the text. The second powder, labeled as **S2**, was prepared by mixing of two pure powders, Ni (99.9% purity) and Ti (99.9% purity). Powders forming our S2 were each manufactured using gas atomization. The manufacturing process of powder S1 is unknown.

The powder S1 had the indicated Ni-Ti composition of 55 wt.% Ni and 45 wt.% Ti, i.e., the theoretical value of the nitinol phase. Guided by the defined weight ratio, we prepared 55 g of Ni and 45 g of Ti measured on a precision scale and then added them together to form the S2 powder.

Prior to the RF-ICP deposition, the S2 powder was homogenized by mixing. For that, both powders placed in plastic containers were put onto a rolling barrel. The S2 powder was therefore mixed continuously for 1 hour, using the contained S2 powder as a counterweight in the process. This ensured that our Ni and Ti components of S2 were evenly distributed in its container volume.

3.2 Deposition process

3.2.1 RF-ICP

For our experiments, we used a TekSpray 15 device manufactured by Tekna (Sherbrooke, Canada). As the torch has a maximum power output of only 15 kW, the system is designed specifically for research and development of ceramic and metallic deposits.

The device can be divided into two sectors, the control panel (CP), and the internal chamber (IC) with all the hardware components. The CP allows the user to set designated parameters with full computerized control and gas level monitoring. The IC includes the main components for coating deposition, such as the plasma torch, deposition chamber, and water cooling, and can be closed with lockable doors composed of metal parts, thus forming a Faraday cage. A view of the device is shown in Fig. 3.1. The original powder feeder supplied with the TekSpray 15 system was not used as it was found the feeding was unstable and not reliable. Instead, an external feeder was used, made by Plasma-Technik from Switzerland. The feeder works on a volumetric feeding principle using a revolving container, providing a steady supply of the powder.

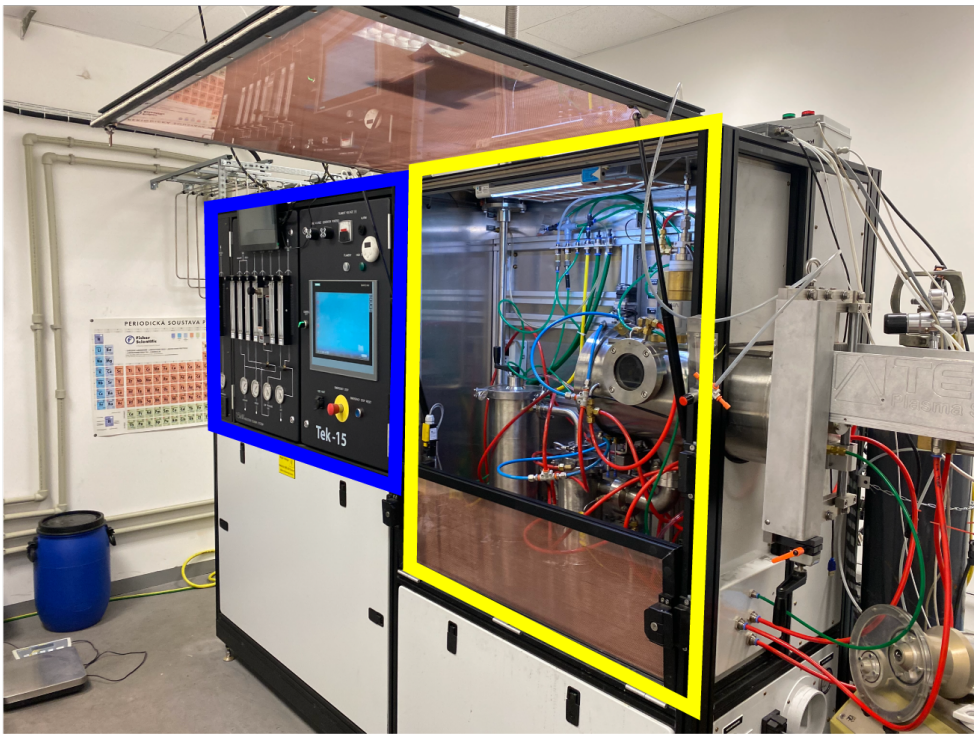

Figure 3.1: Tekna Tekspray 15 with CP in blue area and IC in yellow area.

The main component of the IC is the plasma torch, which is water-cooled and placed vertically above the air-tight deposition chamber. The sealed chamber allows for having a pressurized inert atmosphere and allows visual monitoring through a control window. Among others, this allows checking if the feedstock is fed correctly into the plasma stream or if the plasma stream has unexpected instabilities. The deposition procedure could also be recorded through this control window. A detailed view of the plasma torch and IC is shown in Fig. 3.2.

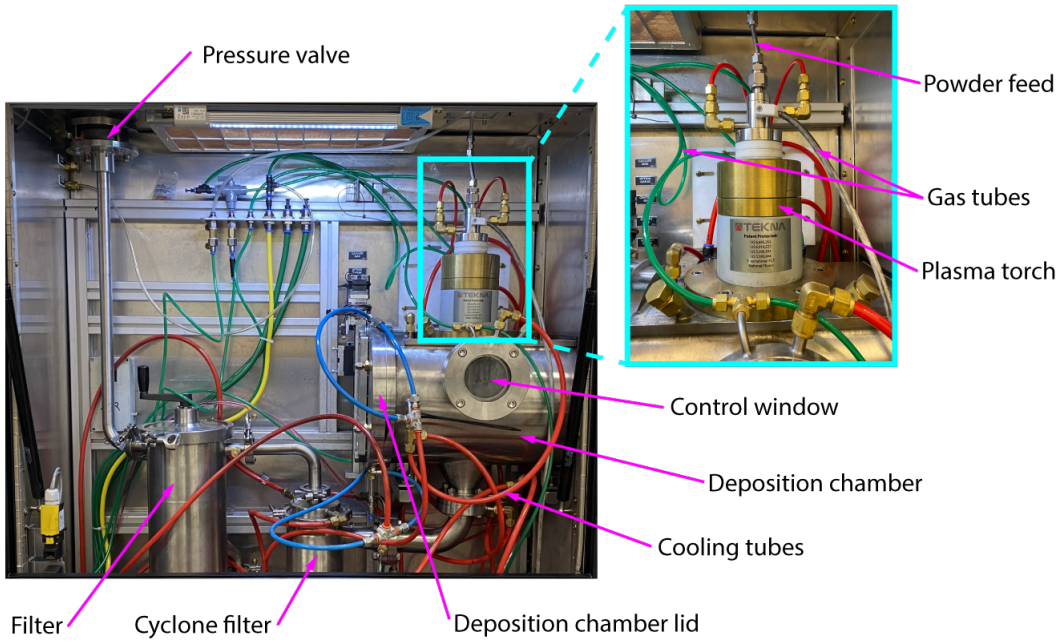

Figure 3.2: The individual components of IC and detailed view of the TekSpray 15 plasma torch.

3.2.2 Coatings deposition

The deposition process took place in the deposition chamber. Identical parameters of the RF-ICP were used for both S1 and S2 powders, including the power of the plasma torch, deposition chamber pressure, and gas flow rates (Table 1). The choice of identical parameters was to isolate the influence of the initial powder properties on the deposited coatings. As a sheath and carrier gas, argon was used, while for central gas, a mixture of argon and hydrogen was used. Argon is a common plasma-forming and powder-carrying gas and is used with hydrogen for better efficiency in the plasma deposition process.

For substrates, we used plates of AISI 304 (austenitic chromium-nickel stainless steel) which were grit-blasted using alumina particles before the deposition. In thermal spraying, grit-blasting is a common procedure for the improvement of adhesion to the substrate by surface roughening and removal of surface oxide layers. After the grit-blasting, the plates were submerged in acetone and cleaned with an ultrasonic cleaner for 10 minutes to remove residual grit. Six substrates were then attached to a hexagonal holder head bolted to the end of a hollow, water-cooled shaft inside the deposition chamber. Before the deposition, the deposition chamber was sealed and vacuum was formed, which was then replaced with an inert atmosphere.

The shaft had a computer-controlled linear displacement in an axial direction and it enabled revolving along this axis. Due to the fixed placement of the torch, movement of the shaft is necessary for the coating deposition process, as visualized in Fig. 3.3. Prior to the deposition, a substrate preheating procedure was carried out to improve the proper splat geometry formation and increase the adhesion. For that, the powder feeding was switched off and the shaft was positioned under the plasma torch. The axial speed and revolutions were set at 0.5 mm/s 20 rpm, respectively. After 80 seconds of preheating, the shaft was returned to its original position away from the torch. The coating deposition phase was then carried out, using a single

pass of the substrates below the torch that lasted 160 seconds. The shaft's movement parameters remained the same as during the preheating step.

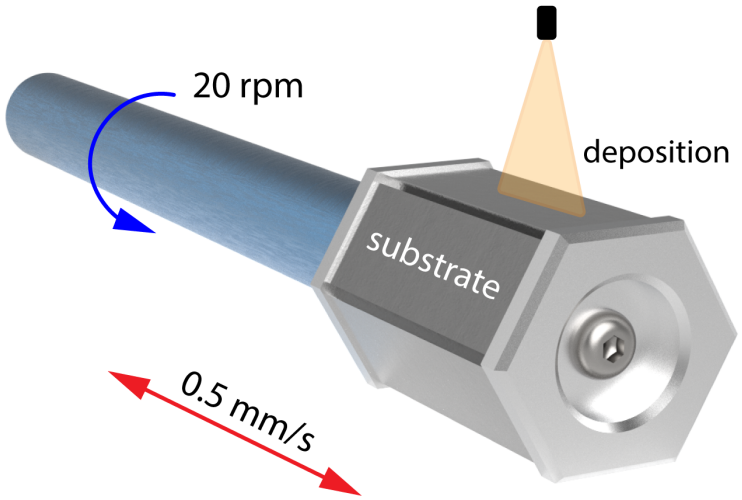

Figure 3.3: Visualization of substrate attachment and shafts movement in the used RF-ICP deposition.

We prepared two coatings labeled **RF1** (from powder S1) and **RF2** (from powder S2). An overview of the used deposition parameters is given in Table 1. The deposition parameters of the RF-ICP were chosen based on previous experience with similar powders. Due to the volumetric-based feeding mechanism of the new feeder and the different powder morphologies, the powder feed rates (with unchanged feeder device parameters) differ.

Table 1: RF-ICP deposition parameters

Parameters	**RF1**	**RF2**
Powder	S1	S2
Powder feedrate (g/min)	2.1	4.5
Plasma torch power (kW)	15	
Deposition chamber pressure (kPa)	103	
Shaft axial speed (mm/s)	0.5	
Shaft rotation speed (rpm)	20	
Preheating time (s)	80	
Powder deposition time (s)	160	
Sheath gas (slmp)	35 (Ar)	
Central gas (slmp)	10 (Ar) + 3.4 (H2)	
Carrier gas (slmp)	8 (Ar)	

3.3 Sample characterization

The particle size distribution measurement of both powders was performed using a Malvern Mastersizer 3000 laser device with a laser diffraction method by wet dispersion (6 measurements for each of the powders from which we calculated their average particle size distribution). The powder properties (morphology by SEM, composition by EDX, phase composition by XRD) were assessed using original particles, as well as their cross-sections. For the former, particles of both S1 and S2 were glued using carbon adhesive tape on a small round target. The cross-sections were prepared by mounting the particles into epoxy resin under a vacuum and cutting the samples in half.

For the coating analysis, cross-section samples of the RF1 and RF2 coatings were prepared. For that, small square-shaped pieces were cut using a diamond blade and embedded in an epoxy resin, again under vacuum.

All samples embedded in the resin were, after curing, grinded using Tegramin-25 (Stuers, Denmark) using FEPA 1200, 2000, and 4000 grit-sized sandpapers. The final step was polishing using 1-µm polycrystalline diamond suspension. After the polishing, the samples were cleaned in isopropanol and dried.

The morphology of both feedstock powders, as well as the microstructure of their cross-section and the cross-section of the corresponding coatings, was studied using SEM (EVO MA 15, Carl Zeiss, Germany) in the backscattered electrons mode to clearly distinguish the two major elements, as well as variations in the chemical composition. EDX (Quantax, Bruker) was used for both area quantification of the composition as well as mapping. The mapping of the distribution of the selected elements (Ni, Ti) was performed to determine the chemical composition and homogeneity of the samples. An additional software, ImageJ, was used to determine the porosity of deposited coatings and to measure the coating thickness from obtained SEM images. The porosity measurement was based on a comparison of areas of different contrast (e.g., pores vs. full material), whereas coating thickness was determined by delineating lines across the coating. The resulting porosity and thickness values were each average of three measurements.

Chapter 4

Results

In this chapter, we will present the results of the analyses of two NiTi powders and the two corresponding coatings deposited using RF-ICP. The results will then be discussed in the next section 5.

4.1 NiTi powders

We analyzed two types of NiTi powders, labeled S1 and S2. The powder S1 was obtained as a commercial NiTi phase powder, while the powder S2 was prepared by mixing of two pure, gas atomized elemental powders in our laboratories. Both powders theoretically had the same weight ratio of 55 wt.% Ni and 45 wt.% Ti, but different morphology and different particle size distribution. The average particle size distributions of S1 and S2 were 58–168 µm and 16–44 µm, respectively (D10–D90). The major difference in the average size of the particles between the two powders is shown in Fig. 4.1 using curves obtained from the average particle size distribution measurements by laser. The morphology of S1 can be described as sponge-like dendrites, shown in Fig. 4.2, whereas S2 has a spherical morphology, shown in Fig. 4.3.

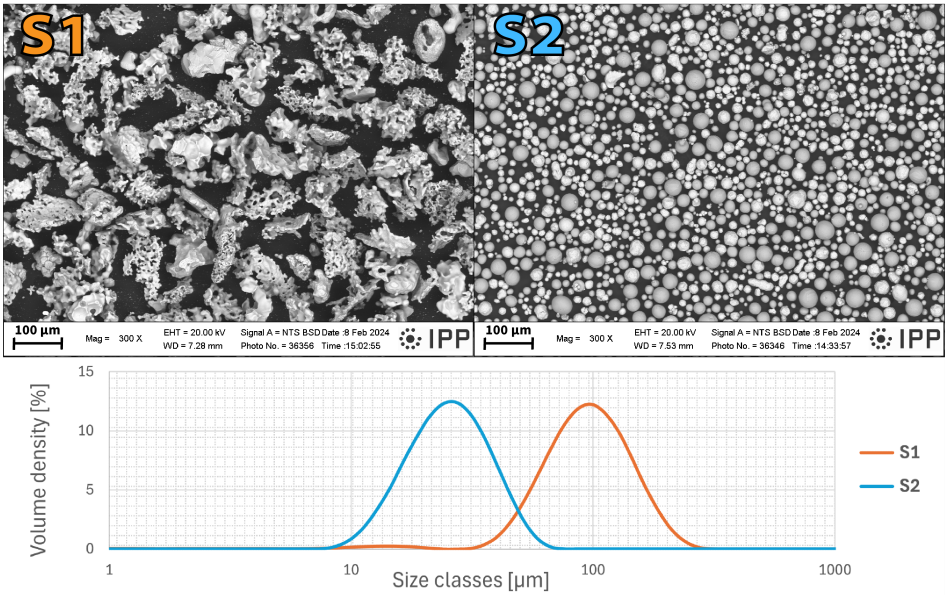

Figure 4.1: Illustration of typical particle sizes of the two used powders and the respective measured volumetric particle size distributions.

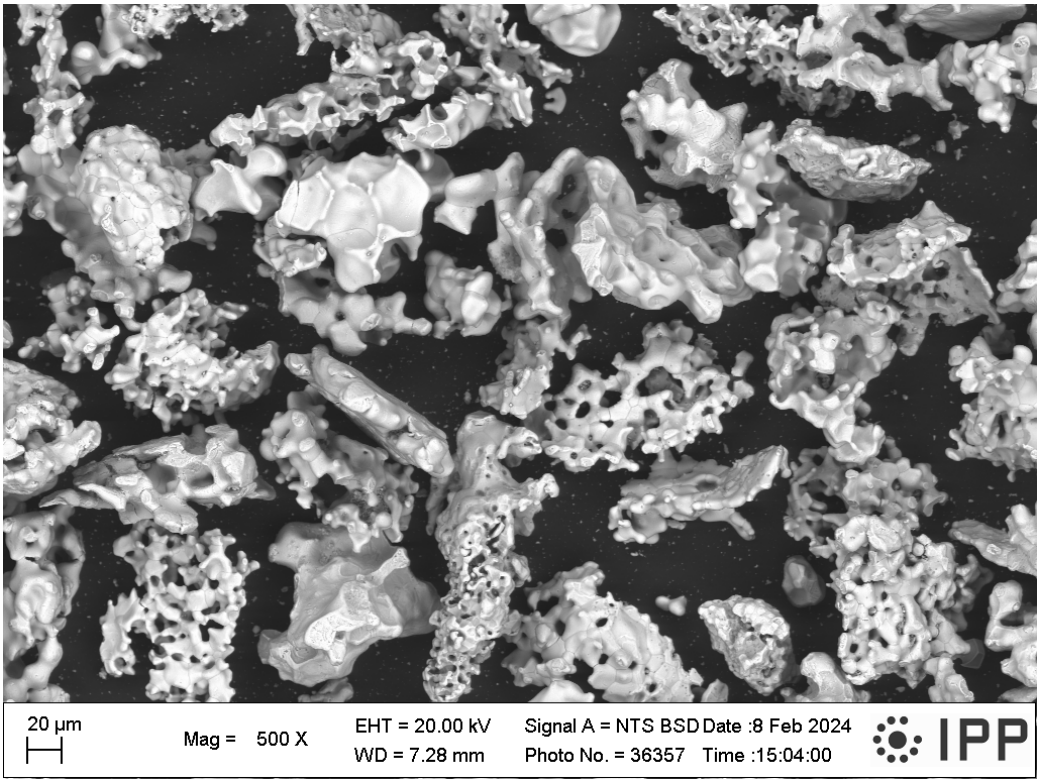

Figure 4.2: Sponge-like morphology of S1 powder.

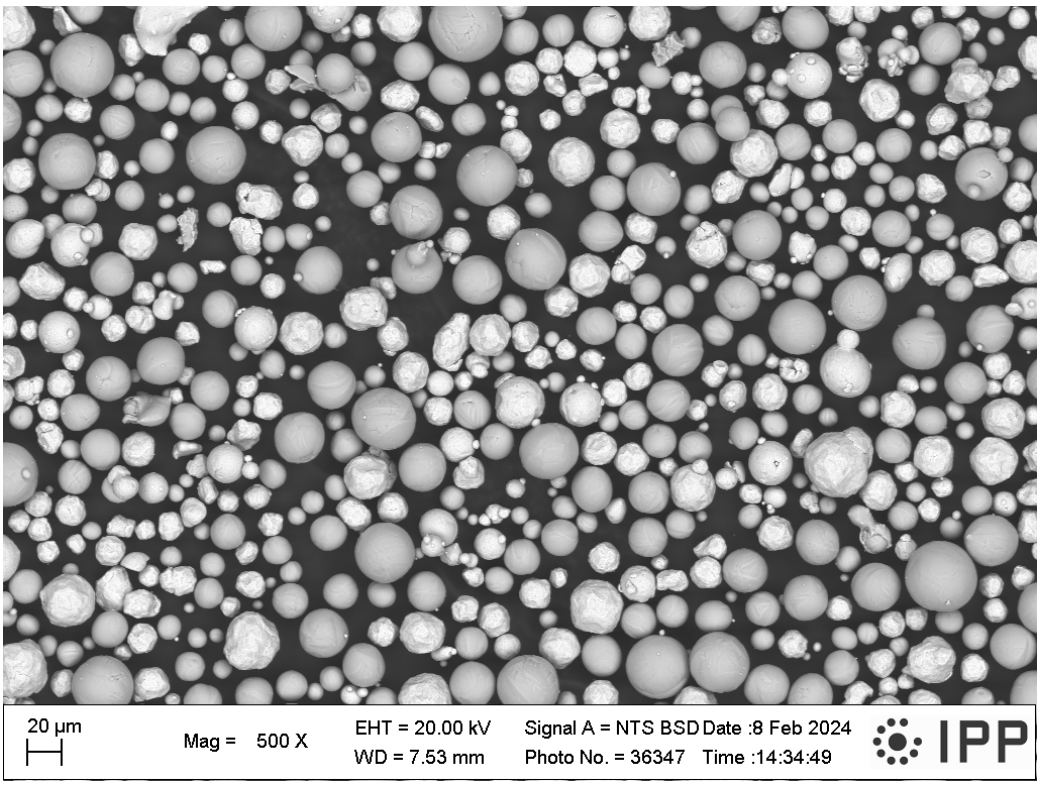

Figure 4.3: Spherical morphology of S2 powder prepared by mixing.

We then performed an EDX analysis of the powders, focusing on the distribution of Ni and Ti and on the weight ratio of Ni-Ti components to see if they corresponded to the initial values. The results for the ratio of the components are given in Table 2.

The component distribution measurements inside the particles were obtained from powder cross-section samples. These EDX mapping results are presented in Figs. 4.4 and 4.5.

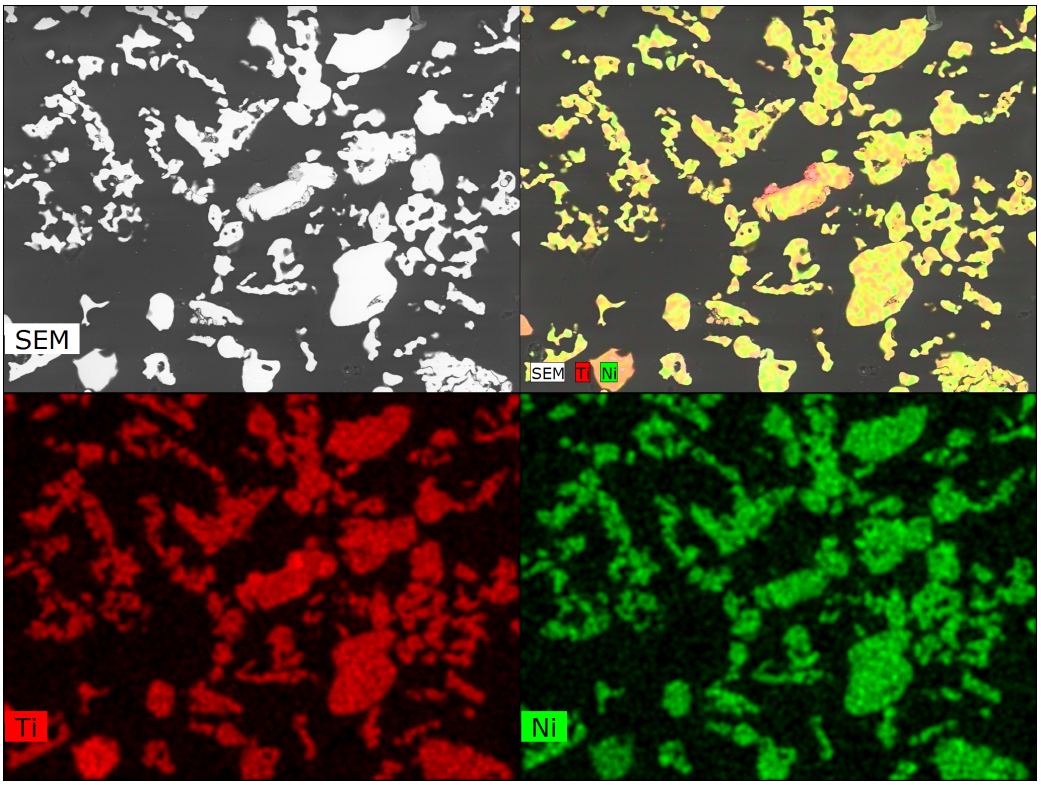

Figure 4.4: Elemental mapping of S1 powder from its cross-section.

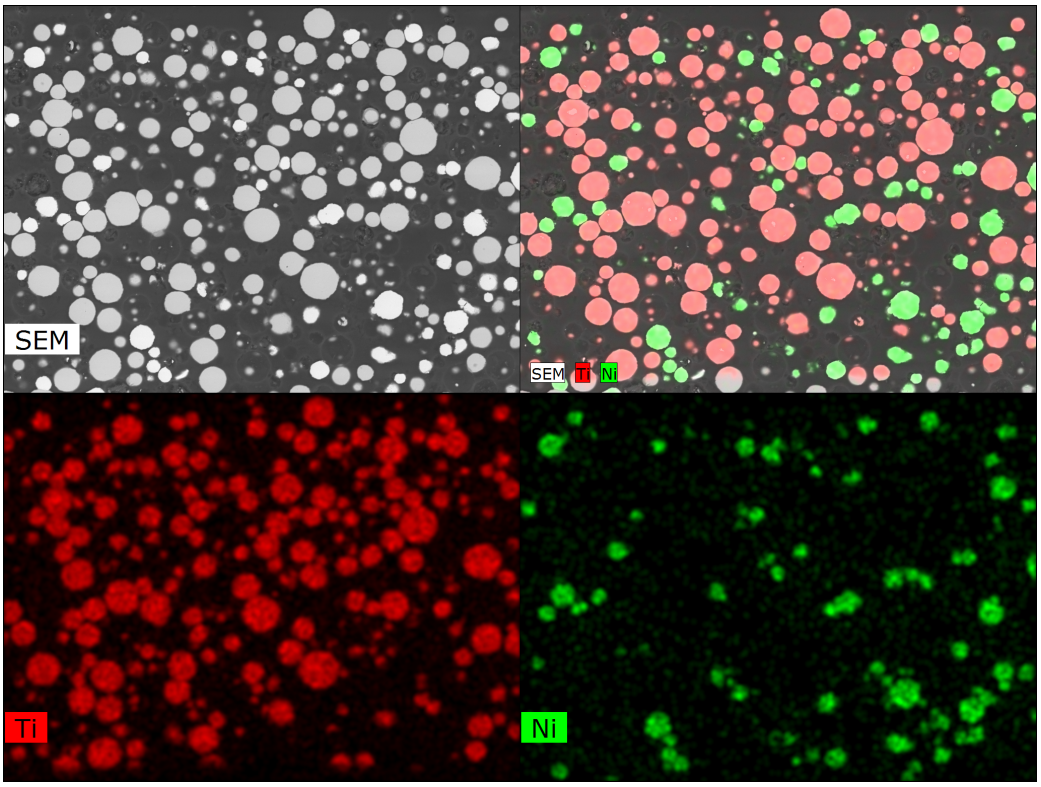

Figure 4.5: Elemental mapping of S2 powder from its cross-section.

4.2 NiTi coatings

We deposited S1 powder using the maximum power output of 15 kW and powder feedrate of 2.1 g/min, with the remaining deposition parameters presented in Table 1.

The resulting RF1 coating was homogeneous and dense, with no clear interface between individual splats, and no unmelted particles (Fig. 4.6). The coatings thickness was approximately uniform across the sample, ranging between 160–200 µm. The porosity of the coating was minimal, specifically 1.4%. The majority of the pores exhibited a very regular, almost ideal spherical shape.

The EDX mapping analysis results shown in Fig. 4.7 further confirmed the coating chemical homogeneity and that the two elements (Ni, Ti) were distributed evenly. The Ni and Ti weight ratio has changed from that of the S1 powder (Table 2). Diffusion of the coating into the substrate was observed at the interface between the two.

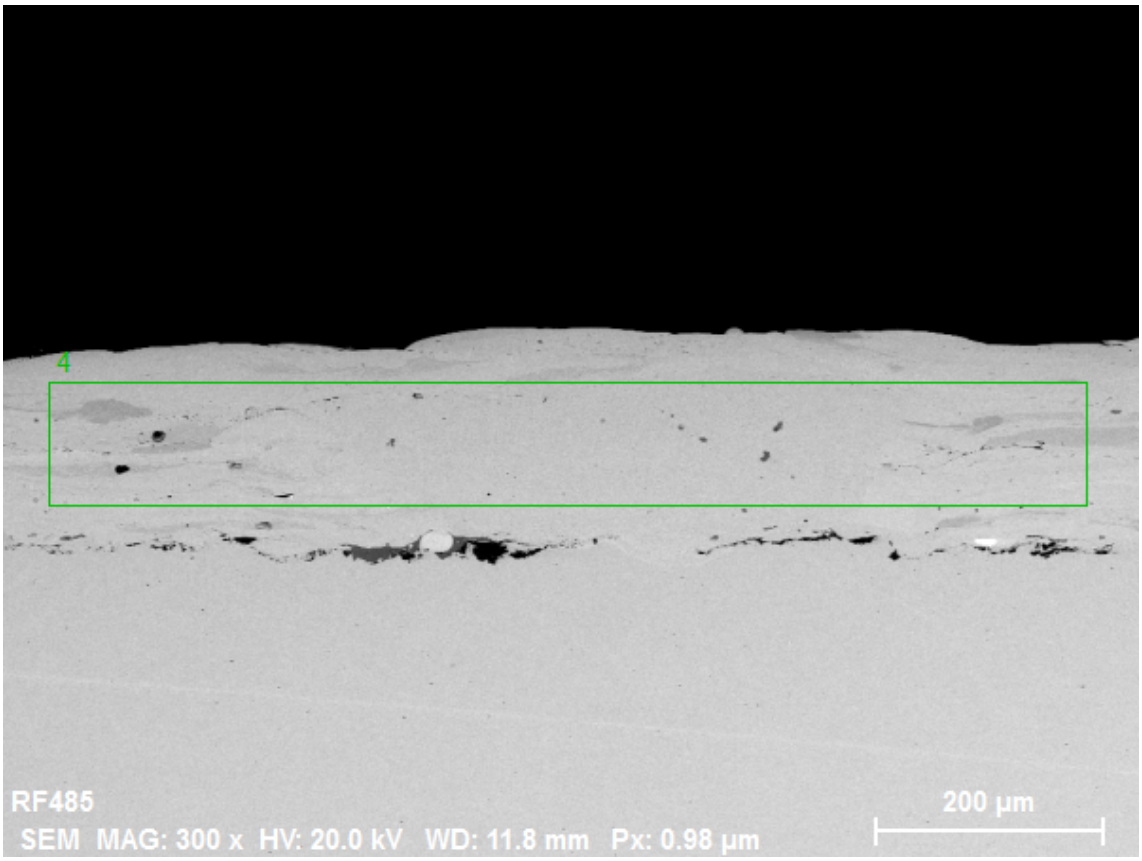

Figure 4.6: Microstructure of the RF1 coating. The green rectangle marks the area of performed EDX analysis.

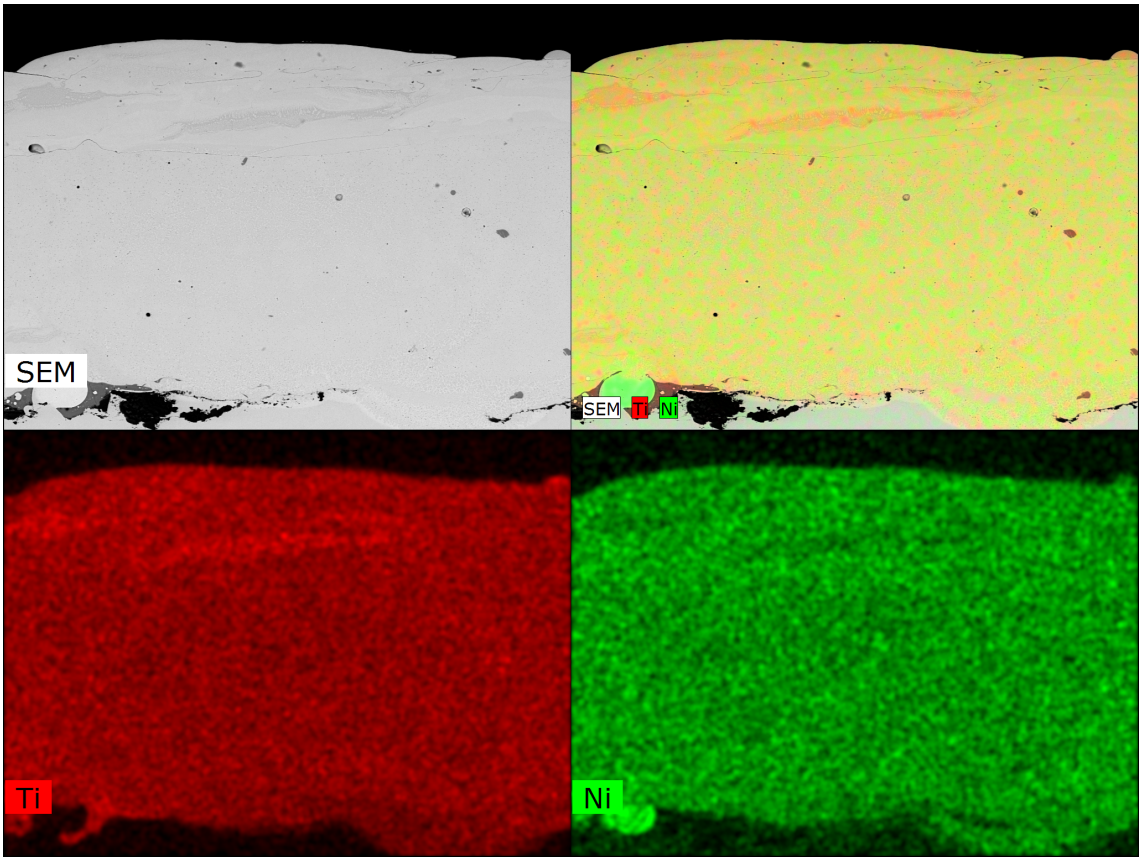

Figure 4.7: EDX elemental mapping of RF1 coating.

For the deposition of the RF2 NiTi coating, we used S2 powder, a mixture of Ni and Ti powders prepared in our laboratories. The RF-ICP deposition procedure and parameters remained the same as for the RF1, but with different powder feedrate of 4.5 g/min. The remaining deposition parameters are presented in Table 1.

The coating was heterogeneous, with clearly recognizable splats of Ni and Ti (Fig. 4.8). No unmelted particles were observed. The coating thickness varied across the sample, ranging between 340–450 µm. Compared to RF1, a larger porosity of 2.4% was observed, with pores present in the coating also exhibiting a spherical shape.

The heterogeneity of the coating was further confirmed by the EDX mapping analysis shown in Fig. 4.9. Some diffusion between the Ni and Ti splats was observed, but little to no diffusion was observed at the coating-substrate interface. The Ni and Ti weight ratio has not changed from the feedstock, as shown in Table 2.

Table 2: Chemical composition of the S1, S2 powders and RF1, RF2 coatings determined by EDX.

Powder	Element	wt.%	**Coating**	Element	wt.%
S1	Ti	50.1	**RF1**	Ti	45.1
	Ni	49.9		Ni	54.9
S2	Ti	59.0	**RF2**	Ti	59.0
	Ni	41.0		Ni	41.0

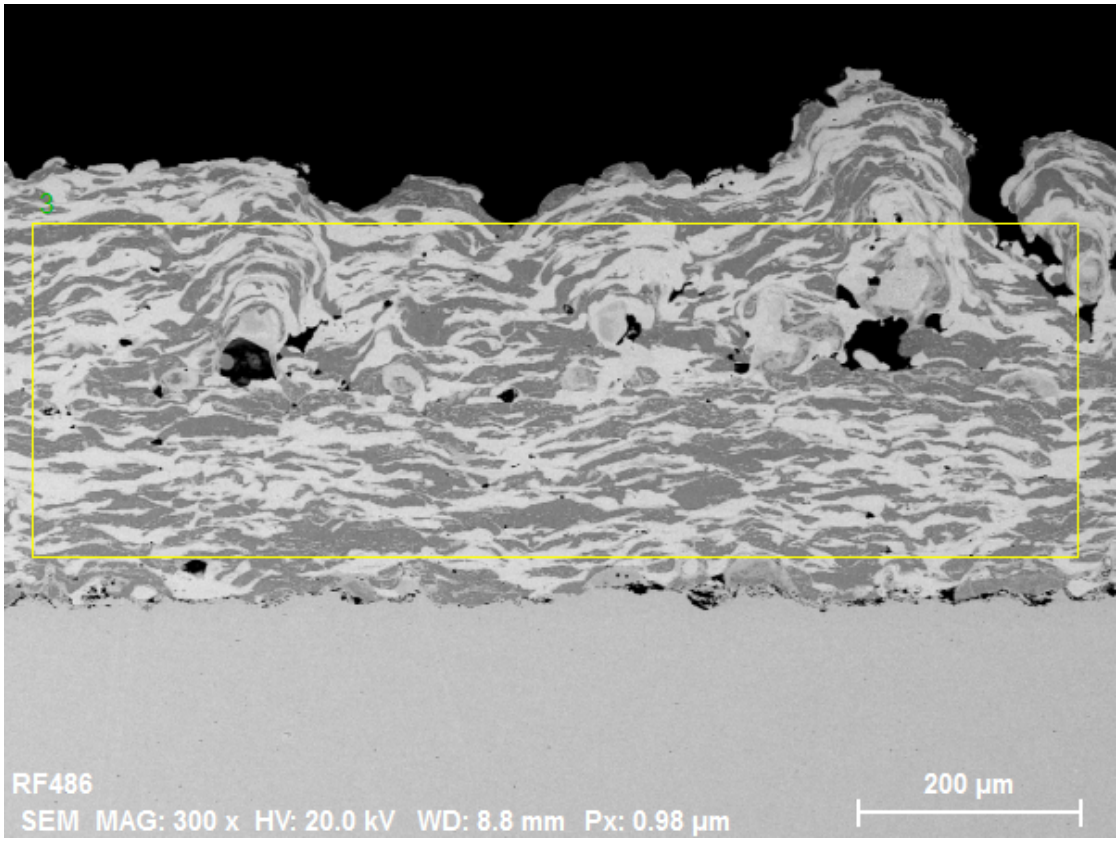

Figure 4.8: Microstructure of the RF2 coating. The yellow rectangle marks the area of performed EDX analysis.

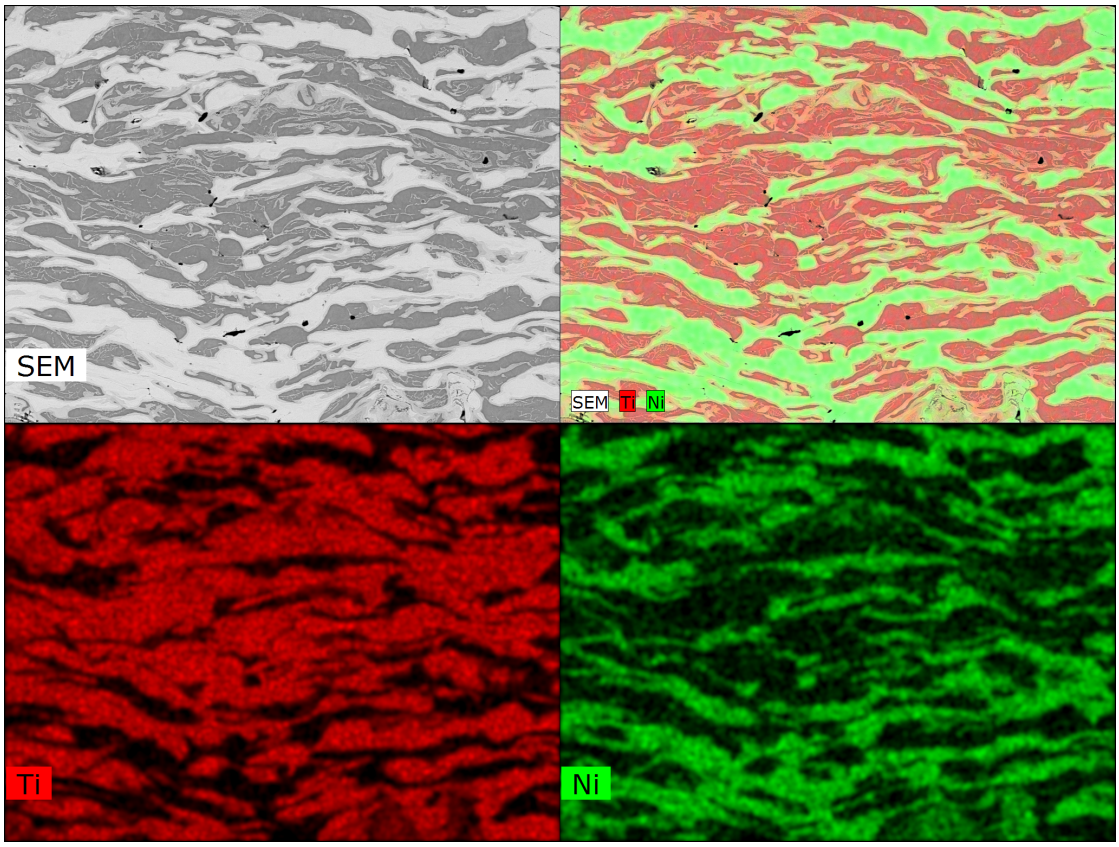

Figure 4.9: EDX elemental mapping of RF2 coating.

4.3 Phase composition

In addition to the initial plan of this thesis, we performed XRD analysis of both powders and coatings to determine the content of the shape-memory-capable NiTi phases and to detect the presence of other phases such as intermetallics.

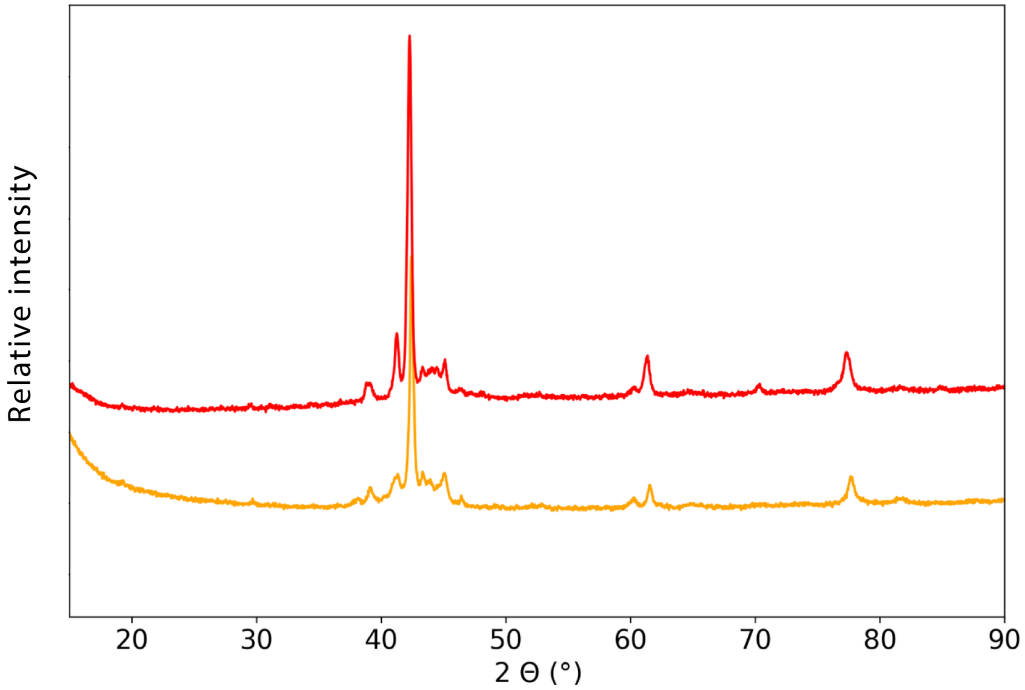

Figure 4.10: XRD analysis results of S1 powder and RF1 coating. S1 is marked by an orange spline and RF1 by a red spline.

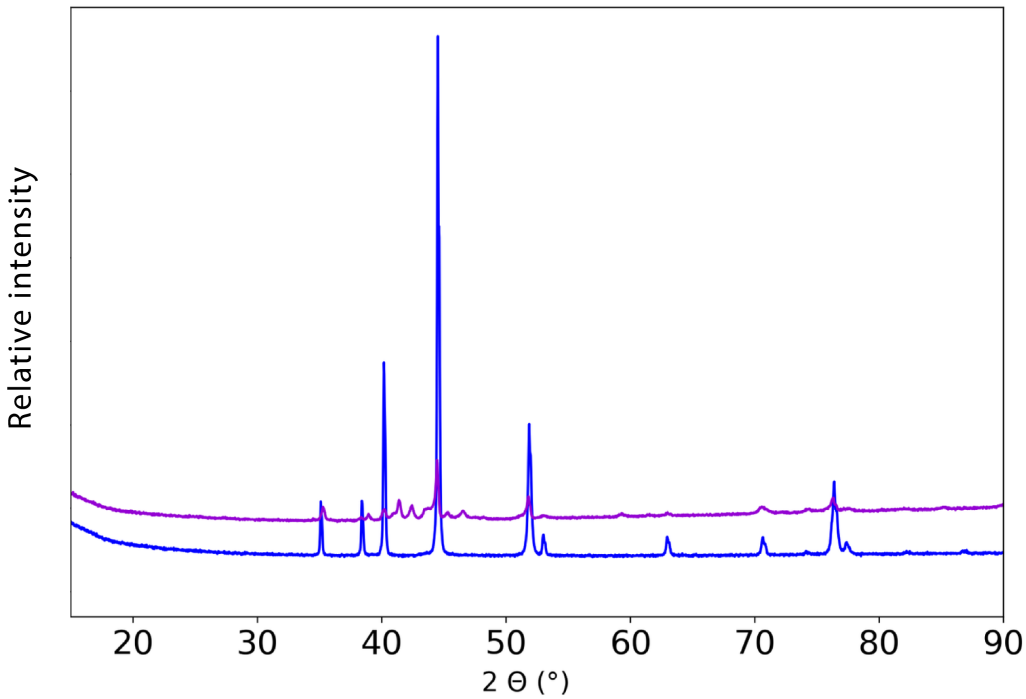

Figure 4.11: XRD analysis results of S2 powder and RF2 coating. S2 is marked by a blue spline and RF2 by a purple spline.

A comparison of XRD analysis results of S1 powder and RF1 coating is shown in Fig 4.10. A mix of austenite and martensite peaks was found in the S1 powder and the deposited RF1 coating. Before the deposition, S1 powder contained mainly austenitic and martensitic phases, with small amounts of $NiTi_2$ and Ni_3Ti intermetallics. After deposition, the amounts of the NiTi austenite phase and $NiTi_2$, Ni_3Ti intermetallics increased slightly at the expense of the martensite. The quantified phase composition comparison between the initial powder and deposited coating is shown in Fig. 4.12.

A comparison of XRD analysis results of S2 powder and RF2 coating is shown in Fig 4.11. Powder S2 was composed of only α-Ti and Ni, no intermetallics were present before the deposition. After the deposition, the amount of α-Ti and Ni decreased in exchange for the formation of Ni_3Ti, $NiTi_2$ intermetallics, and TiH_2. The quantified phase composition comparison between the initial powder and deposited coating is shown in Fig. 4.13.

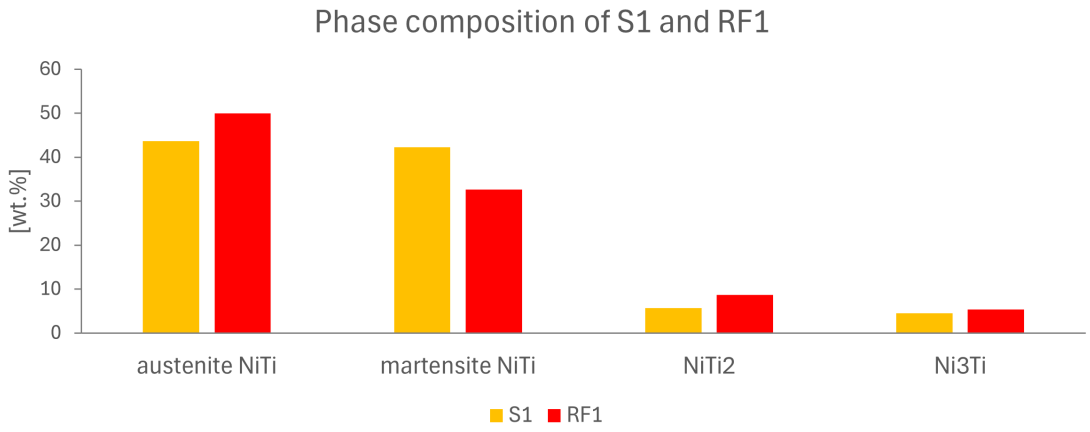

Figure 4.12: Phase composition comparison of S1 powder (orange columns) and RF1 coating (red columns).

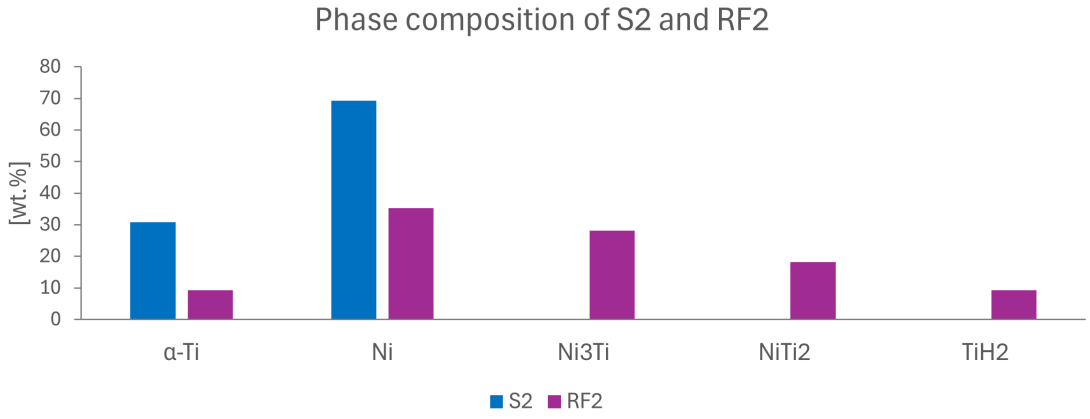

Figure 4.13: Phase composition comparison of S2 powder (blue columns) and RF2 coating (purple columns).

Chapter 5

Discussion

When we compared our particle size distribution results obtained by laser scattering with the SEM images of both powders, we concluded that our measurements were accurate and reflected the actual properties of the powders.

In the curve of powder S1 (Fig. 4.1), a small peak between 10–40 µm was observed. As the shown curve is volumetric, such a result would typically suggest the presence of significantly smaller powder particles, resulting in the bimodal curve distribution. However, no such particles were observed in the SEM. Instead, the peak is most likely a result of the irregular S1 powder morphology. Given their flattened shape, the powder particles reflected the laser differently based on their actual orientation to the beam, causing them to appear smaller when viewed from their thinner face. The manufacturing method of the S1 powder was not provided by the manufacturer, thus the origin of the unique morphology can not be closely commented on.

From the EDX mapping of the powder cross-section (Fig. 4.4), it can be seen that the S1 powder had a uniform distribution of Ni and Ti throughout the entire particle volumes. The manufacturer provided the initial weight ratio of these elements in the powder as Ni 55 wt.% and Ti 45 wt.%, but these values differed from our EDX measurements, with the reality being closer to Ni 50 wt.% and Ti 50 wt.% (Table 2). The answer to the discrepancy between the theoretical and real weight ratios could lie in the unknown manufacturing process of the powder.

To determine the phase composition of the materials and the content of shape-memory-capable NiTi phases, XRD analysis was performed. A comparison of the XRD spectra of the S1 powder with its corresponding deposited coating is shown in Fig. 4.10, while the phase quantification results are provided in Fig. 4.12. The S1 powder contained almost equal amounts of austenite and martensite NiTi phases, specifically 43.6% and 42.2%. As no oxide content was detected in the S1 powder, the manufacturing process of the powder could have taken place in an inert atmosphere. The remaining contents of S1 are intermetallics, specifically $NiTi_2$ and Ni_3Ti, both well below 10 wt.% content. This would suggest a high-temperature production process where diffusion took place, forming these phases. Nevertheless, the majority of the S1 powder comprises a NiTi (nitinol) phase and the powder seems suitable for our RF-ICP deposition.

The powder S2 was prepared in our laboratories from two elemental powders (Ni, Ti) and had a spherical morphology, which was given by the gas atomization manufacturing method of both input powders. In Fig. 4.3, the Ti particles are distinguishable, as they are larger and appear relatively darker than Ni particles due

to their lower atomic number.

From the EDX mapping of the powder cross-section (Fig. 4.5), the powder S2 contained separate spherical particles of Ni and Ti elements, with a predominance of Ti particles. The weight ratio of the elements used for the mixing procedure corresponded to the theoretical ideal nitinol composition, i.e., Ni 55 wt.% and Ti 45 wt.%, but the EDX measurements showed different values of Ni 41 wt.% and Ti 59 wt.% (Table 2). Given that each powder was precisely weighed for the mixture, these deviations from the measured values could probably be based on the shake-down effect: with the two types of particles being relatively different in size and density, they may have sorted in the container during its manipulation. This may have led to seemingly smaller quantities of Ni in the S2 powder in our EDX observations.

In accordance with the XRD analysis and corresponding to the mixed character of the powder, S2 contained only two phases, specifically Ni and α-Ti (69.2 wt.%, 30.8 wt.%, respectively), meaning the NiTi phase was not, understandably, present before the deposition.

Comparing the two input powders, the powder S1 had a sponge-like morphology and noticeably bigger particles (mainly composed of NiTi phase) than powder S2, which was composed of two elemental powders (Ni, Ti) and had spherical morphology. Nevertheless, despite their particle size differences, it turned out that the used 15 kW power of the RF-ICP was sufficient to melt the particles of the S1 powder, while not evaporating the smaller particles of the powder S2.

The individual splat boundaries in the RF1 coating were barely discernible and the coating appeared relatively homogeneous (Fig. 4.6). Combined with the absence of unmelted particles, this would suggest that the RF-ICP deposition parameters were selected well. A small amount of porosity was visible in the coating and along the interface with the AISI 304 steel substrate. The substrate was grit-blasted before the deposition, thus the uneven surface could have contributed to the porosity at the interface and assumedly deteriorated the adhesion of the splats. Better adhesion at this interface could be countered by, e.g., using a modified preheating procedure in the deposition chamber.

The EDX mapping indicated that after S1 deposition, the distribution of Ni and Ti in RF1 was generally uniform across the entire coating, with only a limited amount of regions where either Ni or Ti prevailed slightly, see Fig. 4.7. The measured weight ratio of the deposited RF1 coating differed from that of the S1 powder in a higher content of Ni by approximately 5% (see Table 2). Typically, in plasma spraying, selective evaporation of elements may be triggered when spraying e.g., mixed materials. However, in the case of RF1 coating, this mechanism was most likely not triggered: the selective evaporation of Ti element was unlikely as a) the two elements formed compound phases, and b) the melting temperature of Ti is higher than that of Ni [26]. The area of EDX measurement was sufficiently large too (Fig. 4.6), ruling out insufficient statistical processing. Although the 5% difference is small, it is already above the measurement error, but the reason for this discrepancy could not be reliably determined.

The RF1 coating exhibited changes in the amount of NiTi austenite and martensite NiTi phases, and only a minimal increase in the amount of the two intermetallic phases (see Fig. 4.12). The mutual ratio of the austenite and martensite is not a concern at the current study state as it could be later adjusted by the tunable cooling rates in the deposition chamber under an inert atmosphere or by post-process aging [27]. The increase in the other intermetallic compounds was not significant,

which represents yet another advantage of using the RF-ICP technology for NiTi deposition. As opposed to ambient plasma spray processes, no oxide phases were formed, a feature achieved by the use of the protective atmosphere.

The mixed character of the S2 powder was retained and reflected in the microstructure of the RF2 coating. The individual Ni and Ti splats remained separated, with only very limited diffusion zone formations at their mutual boundaries (see Fig. 4.8). Nevertheless, the interaction of the metals gave rise to the intermetallic phases formation.

This coating character was confirmed by the EDX mapping of RF2 (Fig. 4.9). Here, any major formation of the NiTi austenitic or martensitic phase seemed unlikely, as the Ni and Ti splats are clearly distinguishable. This would suggest that the splats solidified relatively rapidly and there was no major interaction of the molten Ni and Ti materials either in-flight or shortly after their impact at the substrate. The measured weight ratio of the RF2 coating was identical to that of the initial S1 powder. Still, they differed from the theoretical weight ratio of Ni 55 wt.% and Ti 45 wt.% (see Table 2).

After the RF2 coating deposition, the initial phase composition shifted only towards the formation of intermetallics (see Fig. 4.13), which were detected in the XRD analysis. The coating included three new phases: $NiTi_2$ and Ni_3Ti intermetallics and a small content of TiH_2 compound. As indicated by the EDX mapping results, the intermetallic phases formed through the diffusion effects of the two elements in the deposition process. Different from the $NiTi_2$ and Ni_3Ti formation, the TiH_2 hydride has most likely formed during the molten in-flight phase already, due to the high reactivity of pure titanium at high temperatures [28]. As hydrogen was used as one of the system gases, it could have reacted with the Ti, forming the TiH_2 compound. As the diffusion of Ni and Ti elements during the deposition procedure, which would result in the desired NiTi phase (absent in the initial powder), has not occurred during RF2 deposition, the mixing route needs additional processing steps to obtain a coating capable of the shape memory effect. We propose here that, aside from thermal post-processing, a different preparation of the S2 powder could help with the formation of the NiTi phase in the deposition process. If high energy mechanical alloying [29] of the two powders is realized, the material would consist of both Ni and Ti inside individual particles, substantially shortening the diffusion pathways in the subsequent deposition process. This route will be now investigated in the forthcoming study.

A direct comparison of the two coatings RF1 and RF2 illustrates the major influence of the feedstock powder properties. The measured greater coating thickness of RF2 as compared to RF1 (cf. Fig. 4.6, Fig. 4.8) was expected due to the higher powder feedrate. In the relatively homogeneous RF1 coating, any interface between the splats or the substrate was barely visible and the coating exhibited low porosity. In contrast, the heterogeneous RF2 coating clearly showed the substrate interface and individual splats, with somewhat higher porosity compared to RF1. Both coatings exhibited spherical pores, but the RF2 contained less of them. Diffusion to the substrate was observed in the RF1 coating but for the RF2, the diffusion was minimal. Additionally, the distribution of Ni and Ti elements was generally uniform in RF1, but significantly different in RF2 with concentrated areas of Ni and Ti. The contrasting outcomes observed between S1 and RF1 versus S2 and RF2 indicate the necessity for additional preparatory measures when considering future depositions involving S2 powder.

We compared our results with recent studies concerning the deposition of NiTi coatings using plasma spray [30, 31, 32]. In these papers, the coatings were deposited using argon and an admixture of hydrogen as a process gas, thus being similar to our experimental setup. For the coating deposition, NiTi powders (specifically: near equiatomic NiTi [30], separate Ni and Ti [31], and equiatomic Ni and Ti mixture [32]) were deposited onto sandblasted steel substrates.

In the 2009 paper by Guilemany et al. [30], the authors deposited NiTi coatings using a vacuum plasma system (VPS) to study their microstructure and corrosion resistance in contrast to other deposition methods (atmospheric plasma spray and HVOF). The coatings were examined from their polished cross-sections using SEM, EDX, and their phase composition was qualitatively assessed by XRD from their surfaces. The feedstock powders in that study exhibited typical spherical morphology as they were manufactured by gas atomization, and contained two phases, specifically NiTi and $NiTi_2$. The coatings deposited under a low-pressure inert atmosphere were around 85 µm thick and exhibited high density, low oxide contents, and good interface with the substrate, giving rise to very good corrosion resistance properties. The NiTi and $NiTi_2$ phases present in our coatings were also present in the VPS coatings in [30], but their quantification in the coatings as well as in the initial powders has not been presented. Despite the different coating thicknesses, the splat formation of the deposited RF1 coating was similar to the referenced study, with high density and minimal coating porosity. However, the coating-substrate interface was more noticeable in our RF1 deposition.

In the recent 2022 paper by Swain et al. [31], the deposition of NiTi coatings from a mixture of Ni and Ti powders was performed using atmospheric plasma spray to evaluate the mechanical properties of the coatings and to parametrically optimize the process. Cross-sections of the coatings were used for the analysis. Samples were analyzed using SEM, EDX, and XRD. After the experiment, a mathematical model was established for the optimization of the deposition process based on the results of the mechanical properties of the coatings. Before the deposition, the steel substrates were preheated. The deposited coatings contained several phases, specifically Ni, Ti, NiTi, $NiTi_2$, Ni_3Ti, Ni_4Ti_3, TiO, and NiO, with the oxides being present due to the atmospheric deposition. And while, unlike in our study, the NiTi phase was indicated to form from the mixture, the paper [31] only shows two very small peaks of this phase in the XRD spectra, without providing quantification. Nevertheless, such a result suggests that the NiTi phase can be potentially achieved even if a mixture of elemental Ni and Ti powders is used. Also, the present NiTi phase in the final coatings could have been due to the higher power output of the torch (according to the F4MB datasheet [33] maximum power output of 55 kW compared to our 15 kW) used for the deposition, even with the initial powder particles being relatively larger than the particles used for our RF2 deposition. The oxide contents were not observed in our deposited coatings, as the RF-ICP deposition was conducted in an inert atmosphere. The study also offered insight into the formation of the spherical coating porosity also observed in our coatings. The process gas can get trapped during the spreading and cooling of the splats, causing the formation of a round gas bubble, which increases porosity and prospectively also decreases the bond strength.

Preheating procedures were closely studied in the 2022 paper by Roshan et al. [32], where the authors deposited NiTi coatings from a powder mixture using atmospheric plasma spray. The feedstock powders and coatings were analyzed using SEM and XRD. The spherical Ni and angular Ti powders were mixed together to equally

homogenize the powder. The initial phase composition of the powder was only Ni and Ti with no intermetallics. After the deposition, different phases were observed based on the used preheating temperatures. At the highest studied preheating temperature of 400 °C (with torch parameters set to 55 V and 550 A), the coating exhibited Ni, Ti, NiTi, Ni_3Ti, Ni_4Ti_3, TiO_2, Ti_2O, and NiO phases. The formation of the oxides is due to atmospheric deposition, but their quantities cannot be commented on as they have not been shared in the paper. For the particular temperature of 400 °C, the individual splats were completely molten, disk-shaped, and formed a dense coating layer with 0.3% porosity, lower than our RF1 and RF2 coatings. However, the deposited coatings in this paper, which were previously discussed to contain multiple phases, exhibited a certain amount of heterogeneity. Nevertheless, a strong metallurgical bond was observed at the coating-substrate interface at this temperature. Furthermore, coating roughness and porosity decreased with increasing preheating temperatures. This study also observed that substrate preheating temperature improved the interface contact between the splat and substrate. This is in line with our conclusions that a modified preheating procedure might improve the interface character.

Considering the results obtained in our study, it seems the combination of the S1 powder morphology, chemical and phase composition, and the specific RF-ICP deposition parameters are ideal for further research.

Chapter 6

Conclusions

We have designed an experiment in which two different NiTi powders were deposited by RF-ICP on grit-blasted AISI 304 steel substrates under identical deposition parameters. The powders as well as the coatings were then analyzed using SEM, EDX, and XRD methods. From the obtained results, it can be concluded that:

- Properties of the deposited NiTi coatings are strongly dependent on the feedstock powder properties.
- Despite the liquid phase processing, the powder preparation by mixing of separate Ni and Ti powders does not lead to the formation of SMA phases during the deposition. A more intense process such as high energy ball milling could lead to the desired phase formation.
- RF-ICP is suitable for the deposition of NiTi coatings without the introduction of oxide contents during the process. Further, the phase composition does not change significantly and the formation of intermetallics is limited.
- A modified preheating procedure in the deposition chamber was proposed, as it could positively influence the deposited coating properties regarding the density and improved adhesion to the substrate.

Considering its characteristics, powder S1 showed promise for further exploration, as the findings of this experiment reveal its potential as a suitable deposition material.

Given the promising results obtained in this pioneering attempt, further research regarding the shape memory and superelastic properties will be conducted. As the RF-ICP method proved as a suitable choice for producing NiTi coatings with non-detectable oxide content, the next research will aim at controlled sample cooling after the deposition and post-spray annealing.

Nomenclature

Symbols

A_f	Austenite-finish-temperature
A_s	Austenite-start-temperature
M_d	Max. temperature when martensitic structure can no longer be stress induced
M_f	Martensite-finish-temperature
M_s	Martensite-start-temperature

Abbreviations

AC	Alternating current
AM	Additive manufacturing method
CP	Control panel
DC	Direct current
EDX	Energy dispersive X-ray
HVOF	High-velocity oxyfuel spray
ICP	Inductively-coupled plasma
IC	Internal chamber
OWSME	One-way shape memory effect
PE	Pseudoelasticity

PS	Power supply
RF	Radio frequency
RF-ICP	Radio frequency inductively-coupled plasma
SE	Superelasticity
SEM	Scanning electron microscope
SMA	Shape memory alloy
SMC	Shape memory ceramic
SME	Shape memory effect
TWSME	Two-way shape memory effect
VPS	Vacuum plasma system
WAS	Wire arc spray
XRD	X-ray diffraction

List of Figures

List of Tables

Bibliography

1. MOHD JANI, Jaronie; LEARY, Martin; SUBIC, Aleksandar; GIBSON, Mark A. A review of shape memory alloy research, applications and opportunities. *Materials and Design (1980-2015)*. 2014, roč. 56, pp. 1078–1113. ISSN 0261-3069. Available from DOI: https://doi.org/10.1016/j.matdes.2013.11.084.
2. MALIK, Vansh; SRIVASTAVA, Siddharth; GUPTA, Shashwat; SHARMA, Vidit; VISHNOI, Mohit; MAMATHA, T.G. A novel review on shape memory alloy and their applications in extraterrestrial roving missions. *Materials Today: Proceedings*. 2021, roč. 44, pp. 4961–4965. ISSN 2214-7853. Available from DOI: https://doi.org/10.1016/j.matpr.2020.12.860. International Conference on Advances in Materials Processing and Manufacturing Applications.
3. BALASUBRAMANIAN, M.; SRIMATH, R; VIGNESH, L; RAJESH, S. Application of shape memory alloys in engineering – A review. *Journal of Physics: Conference Series*. 2021, roč. 2054, p. 012078. Available from DOI: 10.1088/1742-6596/2054/1/012078.
4. MUDDLE, B.C.; NIE, J.F. Martensite. In: BUSCHOW, K.H. Jürgen; CAHN, Robert W.; FLEMINGS, Merton C.; ILSCHNER, Bernhard; KRAMER, Edward J.; MAHAJAN, Subhash; VEYSSIÈRE, Patrick (ed.). *Encyclopedia of Materials: Science and Technology*. Oxford: Elsevier, 2001, pp. 5189–5193. ISBN 978-0-08-043152-9. Available from DOI: https://doi.org/10.1016/B0-08-043152-6/00901-3.
5. KCIUK, Marek; CHWASTEK, Krzysztof; KLUSZCZYŃSKI, Krzysztof; SZCZYGŁOWSKI, Jan. A study on hysteresis behaviour of SMA linear actuators based on unipolar sigmoid and hyperbolic tangent functions. *Sensors and Actuators A: Physical*. 2016, roč. 243, pp. 52–58. ISSN 0924-4247. Available from DOI: https://doi.org/10.1016/j.sna.2016.02.012.
6. HAMID, Nubailah; AZMI, Ibrahim. Reinforced concrete beam with pseudoelastic SMA hybrid with steel structure for seismic mitigation: A critical review of their prospective, influence factors, drawback and advantages. *IOP Conference Series: Materials Science and Engineering*. 2019, roč. 469, p. 012119. Available from DOI: 10.1088/1757-899X/469/1/012119.
7. AYODE OTITOJU, Tunmise; UGOCHUKWU OKOYE, Patrick; CHEN, Guanting; LI, Yang; ONYEKA OKOYE, Martin; LI, Sanxi. Advanced ceramic components: Materials, fabrication, and applications. *Journal of Industrial and Engineering Chemistry*. 2020, roč. 85, pp. 34–65. ISSN 1226-086X. Available from DOI: https://doi.org/10.1016/j.jiec.2020.02.002.

8. DU, Zehui; ZENG, Xiao Mei; LIU, Qing; SCHUH, Christopher A.; GAN, Chee Lip. Superelasticity in micro-scale shape memory ceramic particles. *Acta Materialia*. 2017, roč. 123, pp. 255–263. ISSN 1359-6454. Available from DOI: https://doi.org/10.1016/j.actamat.2016.10.047.

9. HAGER, Martin D.; BODE, Stefan; WEBER, Christine; SCHUBERT, Ulrich S. Shape memory polymers: Past, present and future developments. *Progress in Polymer Science*. 2015, roč. 49-50, pp. 3–33. ISSN 0079-6700. Available from DOI: https://doi.org/10.1016/j.progpolymsci.2015.04.002. Self-Healing Polymers.

10. BEHL, Marc; LENDLEIN, Andreas. Shape-memory polymers. *Materials Today*. 2007, roč. 10, č. 4, pp. 20–28. ISSN 1369-7021. Available from DOI: https://doi.org/10.1016/S1369-7021(07)70047-0.

11. WEI, Z. G.; SANDSTROM, R.; MIYAZAKI, S. Shape memory materials and hybrid composites for smart systems: Part II Shape-memory hybrid composites. *Journal of Materials Science*. 1998, roč. 33, č. 15, pp. 3763–3783. ISSN 1573-4803. Available from DOI: 10.1023/A:1004674630156.

12. ZHANG, Zhe-Xi; ZHANG, Jie; WU, Honglei; JI, Yuezhen; KUMAR, Dheeraj D. Iron-Based Shape Memory Alloys in Construction: Research, Applications and Opportunities. *Materials*. 2022, roč. 15, č. 5. ISSN 1996-1944. Available from DOI: 10.3390/ma15051723.

13. MAZZER, E. M.; SILVA, M. R. da; GARGARELLA, P. Revisiting Cu-based shape memory alloys: Recent developments and new perspectives. *Journal of Materials Research*. 2022, roč. 37, č. 1, pp. 162–182. ISSN 2044-5326. Available from DOI: 10.1557/s43578-021-00444-7.

14. SAMPATH, Santosh; NGUYEN, Tuan Anh. 7 - NiTi-based ternary shape-memory alloys. In: THOMAS, Sabu; BEHERA, Ajit; NGUYEN, Tuan Anh (ed.). *Nickel-Titanium Smart Hybrid Materials*. Elsevier, 2022, pp. 123–137. Micro and Nano Technologies. ISBN 978-0-323-91173-3. Available from DOI: https://doi.org/10.1016/B978-0-323-91173-3.00006-7.

15. FARBER, Eduard; ZHU, Jia-Ning; POPOVICH, Anatoliy; POPOVICH, Vera. A review of NiTi shape memory alloy as a smart material produced by additive manufacturing. *Materials Today: Proceedings*. 2020, roč. 30, pp. 761–767. ISSN 2214-7853. Available from DOI: https://doi.org/10.1016/j.matpr.2020.01.563. Materials Science: Composites, Alloys and Materials Chemistry.

16. HUANG, Samuel H.; LIU, Peng; MOKASDAR, Abhiram; HOU, Liang. Additive manufacturing and its societal impact: a literature review. *The International Journal of Advanced Manufacturing Technology*. 2013, roč. 67, č. 5, pp. 1191–1203. ISSN 1433-3015. Available from DOI: 10.1007/s00170-012-4558-5.

17. *ChampioNIR™ - Medinol* [https://medinol.com/products/championir/elunir-technical-specifications-2/]. [B.r.]. (Accessed on 01/31/2024).

18. DZOGBEWU, Thywill Cephas; DE BEER, Deon Johan. Additive manufacturing of NiTi shape memory alloy and its industrial applications. *Heliyon*. 2024, roč. 10, č. 1, e23369. ISSN 2405-8440. Available from DOI: https://doi.org/10.1016/j.heliyon.2023.e23369.

19. ROSHAN, Rakesh; PATEL, Swadhin Kumar. 9 - NiTi plasma spray coating. In: THOMAS, Sabu; BEHERA, Ajit; NGUYEN, Tuan Anh (ed.). *Nickel-Titanium Smart Hybrid Materials*. Elsevier, 2022, pp. 151–172. Micro and Nano Technologies. ISBN 978-0-323-91173-3. Available from DOI: https://doi.org/10.1016/B978-0-323-91173-3.00013-4.

20. STELLA, J.; SCHÜLLER, E.; HESSING, C.; HAMED, O.A.; POHL, M.; STÖVER, D. Cavitation erosion of plasma-sprayed NiTi coatings. *Wear*. 2006, roč. 260, č. 9, pp. 1020–1027. ISSN 0043-1648. Available from DOI: https://doi.org/10.1016/j.wear.2005.06.002.

21. DAVIS, Joseph R et al. *Handbook of thermal spray technology*. ASM international, 2004.

22. TOCALO CO., Ltd. *What is thermal spraying? | TOCALO* [https://www.tocalo.co.jp/english/technical/how/]. 2024. (Accessed on 06/01/2024).

23. LOMBARDI, Amadeu Neto; CASTELETTI, Luiz Carlos; TOTTEN, George Edward. Thermal Spray Technologies: An Overview. In: *Encyclopedia of Tribology*. Ed. WANG, Q. Jane; CHUNG, Yip-Wah. Boston, MA: Springer US, 2013, pp. 3607–3617. ISBN 978-0-387-92897-5. Available from DOI: 10.1007/978-0-387-92897-5_684.

24. BOULOS, M. I. RF induction plasma spraying: State-of-the-art review. *Journal of Thermal Spray Technology*. 1992, roč. 1, č. 1, pp. 33–40. ISSN 1544-1016. Available from DOI: 10.1007/BF02657015.

25. BOULOS, Maher I.; FAUCHAIS, Pierre L.; HEBERLEIN, Joachim V. R. Induction Plasma Spraying. In: *Thermal Spray Fundamentals: From Powder to Part*. Cham: Springer International Publishing, 2021, pp. 403–466. ISBN 978-3-030-70672-2. Available from DOI: 10.1007/978-3-030-70672-2_10.

26. ELEMENTS, American. *Melting Point of Metals & Alloys | Toolbox | AMERICAN ELEMENTS ®* [https://www.americanelements.com/meltingpoint.html]. 2024. (Accessed on 06/02/2024).

27. YANG, C.; HUANG, Z.Y.; CHEN, T.; LU, H.Z.; MA, H.W.; LI, H.Z.; YAN, A.; LI, P.X.; HOSODA, H.; CAI, W.S. Large recoverable strains with high recovery rates via cooperative regulation of texture and precipitation in additive manufactured NiTi alloy. *Scripta Materialia*. 2024, roč. 248, p. 116122. ISSN 1359-6462. Available from DOI: https://doi.org/10.1016/j.scriptamat.2024.116122.

28. KREBS, R.E. *The History and Use of Our Earth's Chemical Elements: A Reference Guide*. Bloomsbury Academic, 2006. ISBN 9780313334382. Available also from: https://books.google.cz/books?id=yb9xTj72vNAC.

29. MARTINS, C.B.; SILVA, Genimari; FERNANDES, Bruno; RAMOS, E.; MARDEGAN, D.A.; RAMOS, Alfeu. High-energy ball milling of Ni-Ti and Ni-Ti-Nb powders. *Materials Science Forum - MATER SCI FORUM*. 2006, roč. 530-531, pp. 211–216. Available from DOI: 10.4028/www.scientific.net/MSF.530-531.211.

30. GUILEMANY, J.M.; CINCA, N.; DOSTA, S.; BENEDETTI, A.V. Corrosion behaviour of thermal sprayed nitinol coatings. *Corrosion Science*. 2009, roč. 51, č. 1, pp. 171–180. ISSN 0010-938X. Available from DOI: https://doi.org/10.1016/j.corsci.2008.10.022.

31. SWAIN, B.; CHATTERJEE, S.; MOHAPATRA, S. S.; BEHERA, A. Mechanical Properties Evaluation and Parametric Optimization of Atmospheric Plasma Spray NiTi Coating. *Journal of Materials Engineering and Performance*. 2022, roč. 31, č. 10, pp. 8270–8284. ISSN 1544-1024. Available from DOI: 10.1007/s11665-022-06834-0.

32. ROSHAN, Rakesh; ARORA, Kanwer Singh; BEHERA, Ajit. Effect of substrate temperature on the surface and interface properties of NiTi atmospheric plasma sprayed coating. *Surface Topography: Metrology and Properties*. 2022, roč. 10, č. 3, p. 035034. Available from DOI: 10.1088/2051-672X/ac9072.

33. OERLIKON. *F4MB-XL General Purpose Plasma Spray Gun | Oerlikon Metco* [https://www.oerlikon.com/metco/en/products-services/thermal-spray-equipment/thermal-spray-components/spray-guns/plasma/external-atmospheric-plasma/f4mb-xl/]. 2024. (Accessed on 06/04/2024).